2019-01
January Volume 2 Issue 1
ISSN 2630-5119(Online)

Journal of Atmospheric Science Research

BILINGUAL
PUBLISHING CO.
Pioneer of Global Academics Since 1984

Volume 2 Issue 1 • January 2019 ISSN 2630-5119 (Online)

Journal of Atmospheric Science Research

BILINGUAL PUBLISHING CO.
Pioneer of Global Academics Since 1984

BILINGUAL PUBLISHING CO.
Pioneer of Global Academics Since 1984

BILINGUAL PUBLISHING CO.
Pioneer of Global Academics Since 1984

Volume 2 | Issue 1 | January 2019 | Page 1-41

Journal of Atmospheric Science Research

Contents

Article

Review

Article withdrawl

BILINGUAL PUBLISHING CO.
Pioneer of Global Academics Since 1984

Journal of Atmospheric Science Research
http://ojs.bilpublishing.com/index.php/jasr

ARTICLE

Climatology of Energetics of Cyclones over Indian Seas

Somenath Dutta[1*] Geena Sandhu[2] Sanjay G Narkhedkar[3] Sunitha Devi[4]

1 Meteorological training Institute, India Meteorological Department, Pune-411008, India
2 Met office, INS Hansa, Dabolim, Vasco Da Gama, South Goa, Goa-403801, India
3 Indian Institute of Tropical Meteorology, Dr.Homi Bhaba Road, Pune-411008, India
4 National Weather Forecasting Centre, India Meteorological Department, Mausam Bhavan, Lodi Road, New Delhi-110003, India

ARTICLE INFO

Article history
Received: 2 November 2018
Accepted: 10 December 2018
Published: 7 March 2019

Keywords:
Cyclone
Climatology
Energetics

ABSTRACT

An attempt has been made to bring out a climatology of the energetics associated with the tropical cyclones formed over North Indian Seas, viz., the Arabian Sea (AS) and the Bay of Bengal (BOB). Study period is from 1991 to 2013. During this period a total 88 cyclones that developed over the Indian Seas have been considered. These intense systems are categorized on the basis of their formation region and season of formation. It is seen that during the study period, the frequency of formation of cyclones over BOB is twice that over AS which is consistent with the climatology of the regions. Further, it is noticed that over both the regions, they are more frequently formed in the post monsoon period compared to pre monsoon. The trend analysis of the frequency of cyclones forming over both basins, season wise shows that the overall trend for both basins is of just decreasing type. However, for Arabian Sea; the decreasing trend is more apparent in the post monsoon season, whereas in the case of the Bay of Bengal the decreasing trend is more evident in the pre-monsoon season. Various energy terms, their generation and conversion terms have been computed using NCEP/NCAR reanalysis data. Day to day quantitative analysis of these parameters is studied critically during various stages of the cyclones. The composites of these categorized systems are formed and studied. The formative, intensification and dissipation stages showed variations in their energy terms.

1. Introduction

Understanding of how tropical cyclone activity has varied in the past and will vary in the future is a topic of great interest to meteorologists, policymakers and the general public. Some have expressed concern about the possibility that anthropogenic climate change due to increases in "greenhouse" gases may alter the frequency, intensity and areal occurrence of tropical cyclones. A review of the inter-annual variations of tropical cyclones, their causes and seasonal predictability has been covered by Landsea (2000) [18]. As per the ESCAP-WMO Panel on Tropical Cyclone (2013)[5]; in the North Indian Ocean (over the Bay of Bengal (BOB) and Arabian Sea (AS)), the average number of tropical cyclones formed in a year are just around 5 which accounts for only 6% of the total global average. However, the loss of life, damage to the property and human suffering

**Corresponding Author:*
Somenath Dutta,
Meteorological training Institute, India Meteorological Department, Pune-411008, India.
Email: dutta.drsomenath@gmail.com

 DOI: https://doi.org/10.30564/jasr.v2i1.266

caused by these tropical cyclones and associated storm surges is very high as compared to the other regions. Despite the adverse impact, tropical cyclones are also the main source of precipitation and water availability. The understanding of the trend in the frequency and intensity of tropical cyclones is very important and quite relevant for being both the source of precipitation and cause of damage to life and property.

A lot of work has been carried out by various researchers on these intense systems formed over the Indian seas. Karl & Ludovic (2010) [8], studied the climatology of the intense tropical cyclones over the past three decades from 1990-2008 indicated that there is no increasing trend in the intensity of cyclones since 1980. They also indicated that the reliable data set is too short to highlight multi-decadal variations. Akter and Tsuboki (2014) [1] studied the cyclone frequency distribution over the BOB during 1990-2009 and found that the distribution is bimodal, with a primary post monsoon peak and a secondary pre monsoon peak. They also concluded that the maximum occurrence rate was 0.8 cyclones/year in November. Further, they stated that in the BOB, the trough position and the accompanying low vertical shear are only a precondition for cyclone occurrence. Jamal (2015) [19], while studying the tropical cyclones over the North Indian Seas during 1998-2014 introduced a measure of annual tropical cyclone activity including the effects of frequency, wind speed, and duration. However the investigation of a sample of 92 tropical cyclones showed no signs of the trend within the period of the study with respect to the cyclone activity measure used.

Many investigators found analysis of energetics to be a very useful and interesting tools for diagnosing many atmospheric phenomena dynamically. There are a number of studies on the energetics aspects of onset, progress and maintenance of mean monsoonal circulation viz. Keshavamurty and Awade (1970) [10], Rao & Rajamani (1972) [22] , Krishnamurti & Ramanathan (1982) [11], Krishnamurti (1985) [12], Krishnamurti & Surgi (1987) [13], Yanai et al. (1992) [25], Raju et al. (2002) [21], Rao (2006) [23], Rao and Mohanty (2007) [24] etc. Dutta et al. (2011) [3], Dutta et al. (2012) [4], Krishnamurti et al. (2013) [15], Dutta et al. (2014) [2] etc. The present study focuses on what have been the long-term variations in tropical cyclone activity over the North Indian seas and what may be responsible for such variability with respect to the cyclone energetics. The two basins of the Indian Ocean - the AS and the BOB have been examined in detail. Understanding tropical cyclone variability on inter-annual to inter-decadal timescales has been hampered by the relatively short period over which accurate records are available. Changes in the tropical cyclone databases due to observational platform improvements (and sometime degradations) can often be mistaken as true variations in tropical cyclone activity. Although the Atlantic basin and Northwest Pacific basin have had extensive aircraft surveillance giving valid records going back to at least the late 1940s [Neumann et al. (1993) [20]] and 1950s [JTWC (1974)[6]] . The routine aircraft reconnaissance has not been available for the North Indian Ocean basin and reliable estimates of tropical cyclones only exist in the satellite era beginning in the mid-1960s (Landsea;1993 [16]). Thus, with the instrumental record so limited, it is difficult to make extensive analyses of trends and of the physical mechanisms responsible for the tropical cyclone variability on a global basis. Because of this limitation, most studies on long-term changes in tropical cyclone activity have focused upon the Atlantic and Northwest Pacific. However, even with these limitations, some conclusions can be drawn about past variations in the Indian Ocean basin.

Taking into account of the studies and outcomes of the research carried out by different scientists, an attempt has been made here to study the energy conversion terms of cyclones developed in the Indian Ocean during the recent decade of 1991–2013. Some of the distinguishing features and similarities have been brought out and compared.

2. Data and Methodology

For this study, 6-hourly mean data of temperature field and wind (u, v) and vertical wind (w) reanalyzed data produced by NCEP at grid point (2.5° x 2.5°) have been used. These have been utilized to compute the different energy generation and conversion terms. The period of the study chosen is 1991 to 2013. The energetic terms have been computed on a six-hourly basis beginning from two days before the initial formative stage till the two days post dissipation stages of cyclones over the spatial domain of 2.5°N to 40°N Lat, 40°E to 110°E Lon. The pressure levels considered are from 1000 hPa to 100 hPa i.e. 1000, 850, 700, 600, 500, 400, 300, 250, 150, 100 hPa.

Using these data, following Krishnamurti and Bounua (2000) [14], we have computed zonal & eddy available potential energy [], zonal & eddy kinetic energy , generation of zonal and eddy available potential energy , conversion from eddy available potential energy to eddy kinetic energy , conversion from zonal available potential energy to zonal kinetic energy and conversion from zonal available potential energy to eddy available potential energy . Detail mathematical expression of these energetics parameters are given in table 1.

Frequency of cyclones over AS and BOB for pre mon-

DOI: https://doi.org/10.30564/jasr.v2i1.266

soon and post monsoon have been plotted in the form of a line graph for the period 1991 to 2013. A linear trend is also computed and analyzed for these frequency plots. Bar Graphs of each of the computed energetic terms, generation as well as conversion terms for each cyclone have been plotted for the pre monsoon and post monsoon seasons of both, AS and BOB. Day to day quantitative analysis of these parameters has been studied critically during various stages of the cyclones. Daily mean values of above mentioned energy conversion terms have been calculated by taking the average of the computed 6-hourly energetics data. Then the composites for the above obtained data have been plotted for pre monsoon and post monsoon of the Arabian Sea and Bay of Bengal for the period 1991 to 2013.

The above mentioned composites have been compared, both season wise and basin wise.

Table 1. Detail mathematical expression of energetics parameters

Mathematical expression of different terms	
A_Z	$\int_{100}^{P_s} \frac{\overline{T^{*2}}}{2\sigma} dp$
A_E	$\int_{100}^{P_s} \frac{\overline{T'^2}}{2\sigma} dp$
K_Z	$\frac{1}{2g}\int_{100}^{P_s} \overline{([u]^2+[v]^2)} dp$
K_E	$\frac{1}{2g}\int_{100}^{P_s} \overline{(u'^2+v'^2)} dp$
$G(A_Z)$	$\frac{R_d}{C_p}\oint \frac{[\theta]^*[\dot{Q}]^*}{p\left(-\frac{\partial\overline{\theta}}{\partial p}\right)} dm$
$G(A_E)$	$\frac{R_d}{C_p}\oint \frac{\theta'\dot{Q}'}{p\left(-\frac{\partial\overline{\theta}}{\partial p}\right)} dm$
$C(A_E,K_E)$	$-\frac{1}{g}\int_{100}^{P_s} \frac{R}{p}\overline{\omega' T'} dp$
$C(A_Z,K_Z)$	$-\frac{1}{g}\int_{100}^{P_s} \frac{R}{p}\overline{\omega^* T^*} dp$
$C(K_Z,K_E)$	$\left\{\begin{array}{l} \int_{100}^{P_s}\left[\cos\frac{\varphi u' v' \partial}{a\partial\varphi}\left[\frac{[u]}{\cos\varphi}\right]\right] dp \\ + \int_{100}^{P_s}\overline{\left[v'^2\frac{\partial[v]}{a\partial\varphi}\right]} dp + \int_{100}^{P_s}\overline{\left[\frac{\tan\varphi}{a}u'^2[v]\right]} dp \\ + \int_{100}^{P_s}\overline{\left[\frac{\omega' u' \partial[u]}{\partial p}\right]} dp + \int_{100}^{P_s}\overline{\left[\frac{\omega' v' \partial[v]}{\partial p}\right]} dp \end{array}\right\}$
$C(A_Z,A_E)$	$-\int_{100}^{P_s}\left[\frac{1}{\sigma}v'T'\frac{\partial T^*}{a\,\partial\emptyset}+\frac{1}{\sigma}\omega' T'\frac{\partial T^*}{\partial p}\right] dp$

3. Results and Discussion

The results obtained for frequency/trend analysis and composite analysis are discussed separately in the following sections.

3.1 Frequency/Trend Analysis

The annual tropical cyclone frequency distribution over Indian seas, during 1991-2013 is shown in Fig. 1. It is clearly seen from the figure that distribution is bimodal and consistent with previous reports (Akter and Tsuboki, 2014 [1] and references therein). The primary peak is in November whereas the secondary peak is in May. Frequency and Trend analysis for the cyclones developed from 1991 to 2013 during pre monsoon and post monsoon and in both basins are shown in Fig. 2 (a-d) respectively.

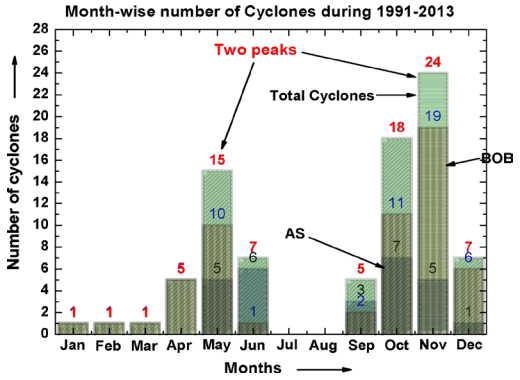

Figure 1. Annual tropical cyclone occurrence frequency over AS and BOB

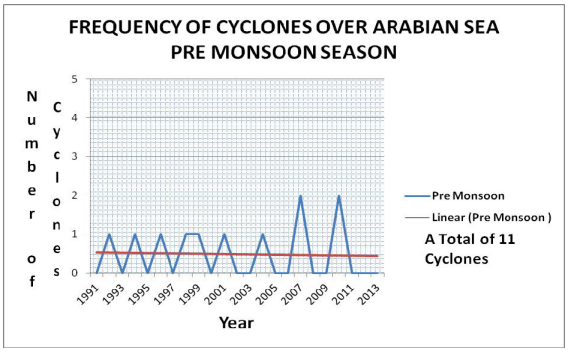

Figure 2 (a). Frequency of cyclones over Arabian Sea – pre monsoon

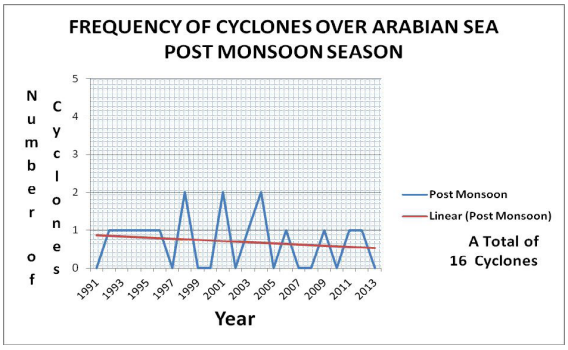

Figure 2 (b). Frequency of cyclones over Arabian Sea – post monsoon

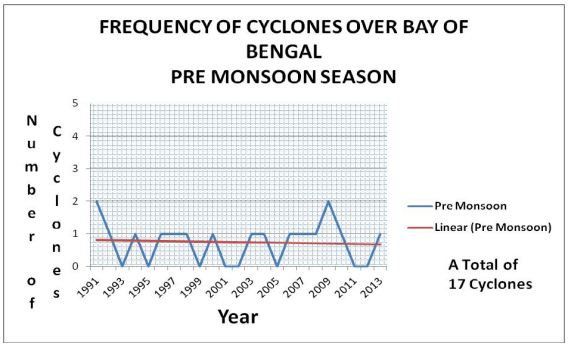

Figure 2 (c). Frequency of cyclones over Bay of Bengal– pre monsoon

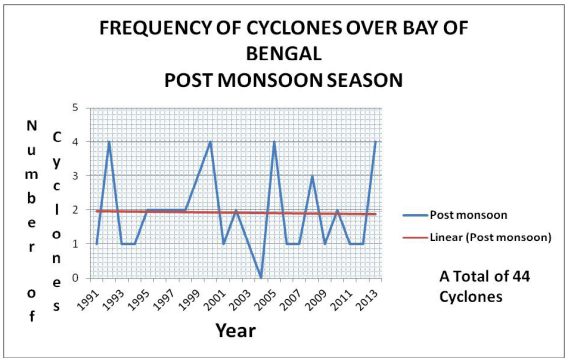

Figure 2 (d). Frequency of cyclones over Bay of Bengal– post monsoon

3.1.1 Frequency Analysis

It is observed that a total of 61 cyclones developed in the BOB during the period from 1991 – 2013 while 27 developed in the AS. Also the frequency of events was much higher for the post monsoon season rather than the pre monsoon season. The frequency of cyclones over AS is observed to range from 0 to 2 cyclones in a year during the period from 1991 to 2013 for both seasons. On the other hand, for the BOB number of cyclones developed in a year for the same period range from 0 to 2 for the pre monsoon season and 0 to 4 for the post monsoon season. This shows that the maximum frequency of formation of cyclones over BOB is twice that over AS. Further, it is noticed that over BOB they are more frequently formed in the post monsoon season compared to pre monsoon season.

3.1.2 Trend Analysis

The general trend for both basins is found to be of just decreasing type for both seasons. However, for AS; the decreasing trend is more apparent in the post monsoon season, whereas in the case of BOB the decreasing trend is more evident in the pre monsoon season.

3.2 Composite Analysis

3.2.1 Composite Analysis of C (Ae, Ke)

Daily Composite Analyses of C (Ae, Ke) for pre and post monsoon over both basins viz. AS and BOB are shown in Fig. 3 (a,b) and Fig. 4 (a,b) respectively. It can be seen that during the formative and mature stage, most cyclones are showing generation of Ae with C(Ae,Ke) negative. Generation of Ke from Ae with C(Ae,Ke) positive is occurring only in the dissipating stage. Ke is converted to Ae when the contour trough lags behind the thermal trough. In this case the trough gets intensified instead of moving, Holton (2004) [9]. Thus the negative C(Ae,Ke) in the composite signifies that in the formative and mature stage of cyclones under study, Ae was generated at the cost of Ke on a daily scale in both seasons, which resulted in its intensification. The positive C(Ae,Ke) in the composite is seen in the dissipating stage indicating that the cyclone gained movement in this stage.

However, in the Bay of Bengal some cyclones are showing C (Ae,Ke) as positive all throughout their lifecycle, Fig. 3 (b) and Fig. 4 (b). This indicates that although Ae is generated at the cost of Ke in most cyclones over both basins; there are certain cyclones that developed in the Bay of Bengal, which did not follow this pattern and there was a continuous generation of Ke at the cost of Ae. This denotes that they gained movement from the formative stage itself and continued gaining movement till the end of their lifecycle.

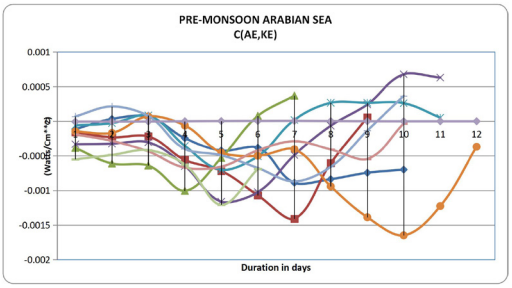

Figure 3 (a). Daily mean composite of C(Ae,Ke) – pre monsoon: Arabian Sea

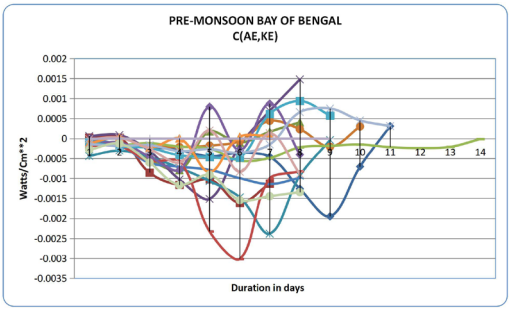

Figure 3 (b). Daily mean composite of C(Ae,Ke) – pre monsoon: Bay of Bengal

DOI: https://doi.org/10.30564/jasr.v2i1.266

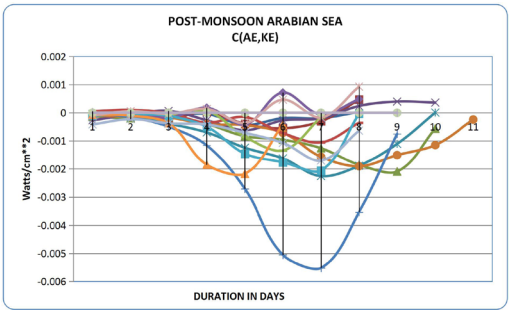

Figure 4 (a). Daily mean composite of C(Ae,Ke) - post monsoon: Arabian Sea

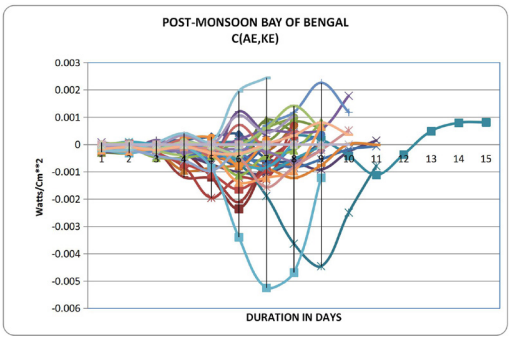

Figure 4 (b). Daily mean composite of C(Ae,Ke) - post monsoon: Bay of Bengal

3.2.2 Composite Analysis of C (Az,Kz)

Daily Composite Analyses of C (Az,Kz) for pre and post monsoon over both the basins viz. AS and BOB are shown in Fig. 5 (a,b) and 6 (a,b) respectively. It can be seen that in the pre monsoon season during the formative stage and dissipating stage, most cyclones are showing generation of Kz with C (Az,Kz) positive. Generation of Az from Kz with C (Az,Kz) negative is occurring in the mature stage. This pattern of energy conversion is similar for both the basins. This indicates that at the time of cyclone intensification over both basins; during pre monsoon, weakened mean meridional circulation prevails. From its expression, it is clear that C (Az,Kz), [equation (13)] represents the strength of mean meridional circulation, which is due to rising motion over the warm latitudinal zone and sinking motion over the cold latitudinal zone. Thus the negative C (Az,Kz) in the mature stage in both seasons indicates the weakened effect of mean meridional circulation, i.e, Hadley circulation and development of Az at the expense of Kz. The decrease in Kz could be attributed to friction. However, some cyclones in the post monsoon season show generation of Kz at the expense of Az all throughout their life cycle with C (Az,Kz) positive. This signifies the strong mean meridional circulation and subsequent strong mean flow at the time of the lifecycle of these cyclones.

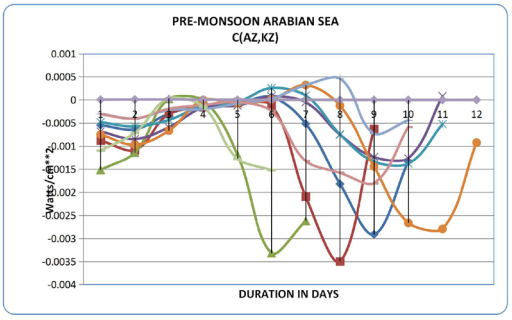

Figure 5 (a). Daily mean composite of C(Az,Kz) – pre monsoon: Arabian Sea

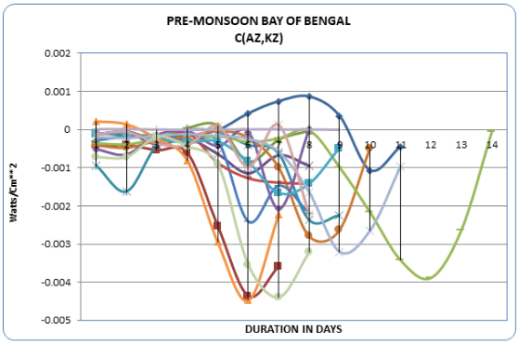

Figure 5 (b). Daily mean composite of C(Az,Kz) – pre monsoon: Bay of Bengal

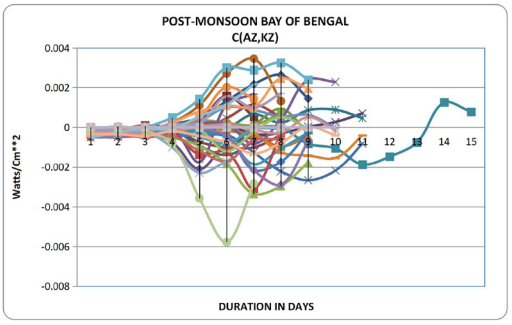

Figure 6 (a). Daily mean composite of C(Az,Kz) – post monsoon: Bay of Bengal

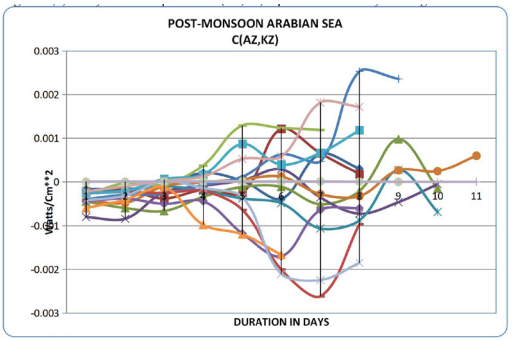

Figure 6 (b). Daily mean composite of C(Az,Kz) – post monsoon: Arabian Sea

3.2.3 Composite Analysis of C(Kz,Ke)

Daily Composite Analyses of C (Kz, Ke) for pre and post

monsoon over both basins viz. AS and BOB, are shown in fig. 7 (a,b) and 8 (a,b) respectivly. It can be seen that during the formative and mature stage, most cyclones are showing generation of Ke with C (Kz,Ke) positive. Generation of Kz from Ke with C (Kz,Ke) negative is occurring only in the dissipating stage. However, in the post monsoon some cyclones are showing C (Kz,Ke) as negative with the generation of Kz from Ke in mature stage and generation of Ke at the expense of Kz in the dissipating stage. This indicates that over both basins generation of maximum wind speed at the expense of Kz during pre monsoon and post monsoon was during formative and mature stages. Although there were some cyclones (over both basins) that developed in the post monsoon, which showed a departure from this pattern and maximum wind speed was generated at the cost of Kz only during the dissipating stage. Enhancement of Ke at the expense of Kz during formative and mature stage indicates that the systems are gaining maximum wind speed at the expense of zonal mean flow. It can also be seen that during the mature stage C (Az,Kz) was negative with steady decrease in Kz. Thus the weakened mean meridional circulation might have influenced significantly on the gain of maximum wind speed for the cyclones. Further, the term C (Ae,Ke) was also negative at the same time, Figs. 3 (a,b) and 4 (a,b). This indicates cyclones were gaining Ke solely at the expense of Kz. However, during the dissipating stage, composites indicate the generation of Kz from Ke with C(Kz,Ke) term as negative. At the same time positive C(Az,Kz) was also observed, indicating an increase in mean zonal flow at the expense of both Az and Ke, Figs. 5 (a,b) and 6 (a,b).

However, some cyclones in the post monsoon showed an opposite pattern with the generation of Kz at the expense of Ke during the formative and mature stage with C(Kz,Ke) term negative and generation of Ke from Kz during the dissipating stage with C(Kz,Ke) term positive. The production of Kz at the expense of Az was also seen in some cyclones at the same time with C(Az,Kz) positive all throughout. So for these cyclones gain in mean zonal flow was again at the expense of Az and Ke. Further, during dissipation these cyclones gained maximum wind speeds (Ke) at the expense of the increased mean zonal flow (Kz).

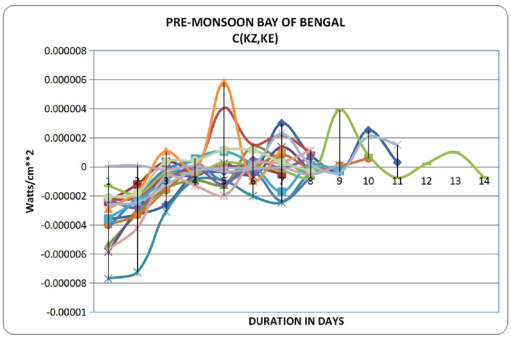

Figure 7 (a). Daily mean composite of C(Kz,Ke) – pre monsoon: Bay of Bengal

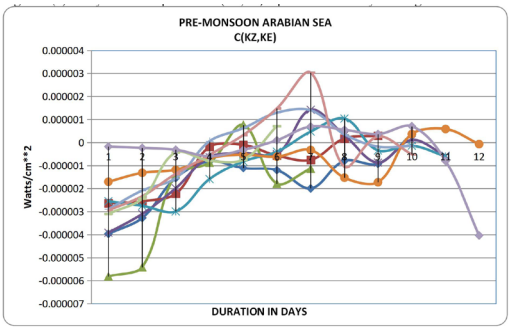

Figure 7 (b). Daily mean composite of C(Kz,Ke) – pre monsoon: Arabian Sea

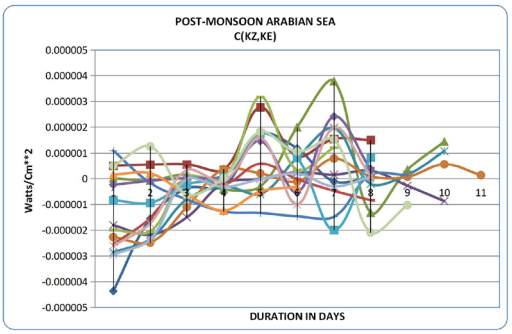

Figure 8 (a). Daily mean composite of C(Kz,Ke) – post monsoon: Arabian Sea

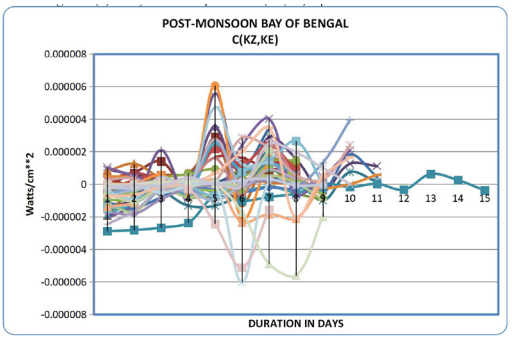

Figure 8 (b). Daily mean composite of C(Kz,Ke) – post monsoon: Bay of Bengal

3.2.4 Composite Analysis of C(Az,Ae)

Daily Composite Analyses of C (Az,Ae) for pre and post monsoon over both the baisns viz. AS and BOB are shown in Fig. 9 (a,b) and 10 (a,b) respectively. Although no distinct pattern can be seen from the figures, the evolution of C(Az,Ae) for a particular cyclone can be studied. The time evolution of C(Az,Ae) for cyclonic storm 'Yemyin' which developed over the Arabian Sea in the Pre monsoon season with lifecycle 25 – 26 June 2007 and severe cyclonic storm 'Alia' which developed over Bay of Bengal in the with lifecycle 23 – 26 May 2009 is shown in Fig 11 (a,b). The time evolution of C(Az,Ae) for cyclonic storm which developed over Arabian Sea in post monsoon season with lifecycle 11

DOI: https://doi.org/10.30564/jasr.v2i1.266

– 17 Oct 1998 and very severe cyclonic storm which developed over Bay of Bengal with lifecycle 23 – 28 Dec 2000 is shown in Fig 12 (a, b). The figures indicate the generation of Ae from Az with C(Az,Ae) positive and generation of Az from Ae with C(Az,Ae) negative is occurring only in the dissipating stage. Generation of Ae from Az with C(Az,Ae) positive indicates the influence of mid latitude baroclinic circulation. [Dutta et. al, (2011) [3]]. Thus the daily mean composite suggests that the mid latitude baroclinic circulation might have influenced significantly on the development and intensification of the selected cyclones. It can be observed that at the same time there was generation of Ae from Ke as well with C (Ae,Ke) negative. However, negative C (Az,Ae) during dissipation indicates that there was hardly any influence of mid latitude baroclinic circulation.

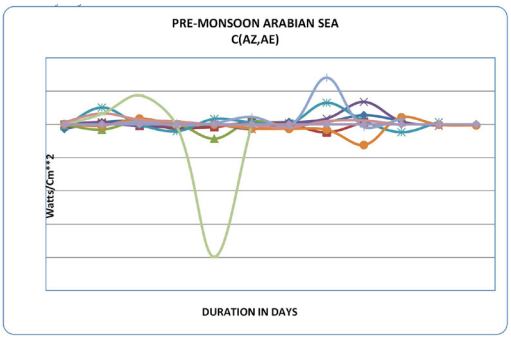

Figure 9 (a). Daily mean composite of C(Az,Ae) – pre monsoon: Arabian Sea

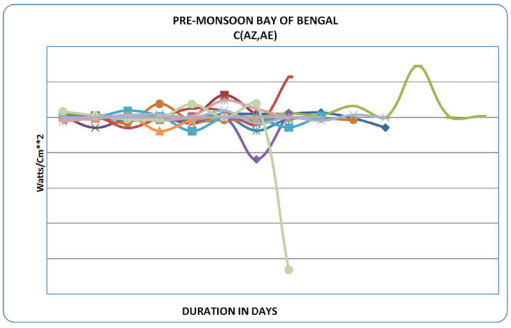

Figure 9 (b). Daily mean composite of C(Az,Ae) – pre monsoon: Bay of Bengal

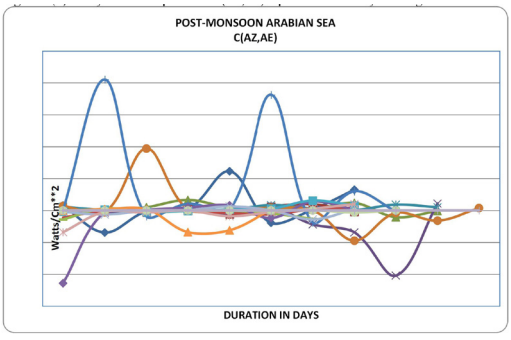

Figure 10 (a). Daily mean composite of C(Az,Ae)– post monsoon: Arabian Sea

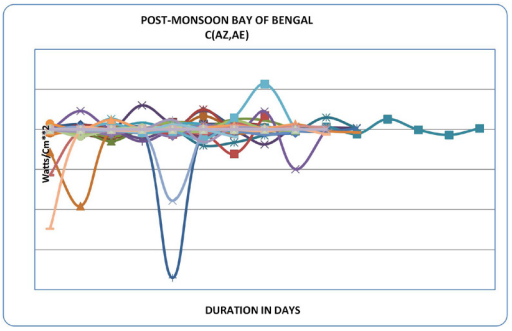

Figure 10 (b). Daily mean composite of C(Az,Ae)– post monsoon: Bay of Bengal

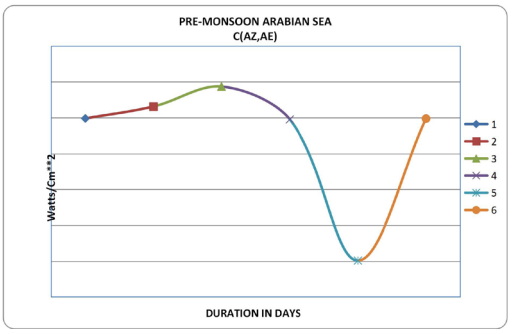

Figure 11 (a). Daily mean of C(Az,Ae) case wise – pre monsoon: Arabian Sea

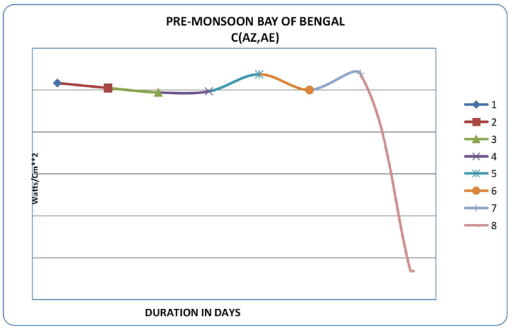

Figure 11 (b). Daily mean of C(Az,Ae) case wise – pre monsoon: Bay of Bengal

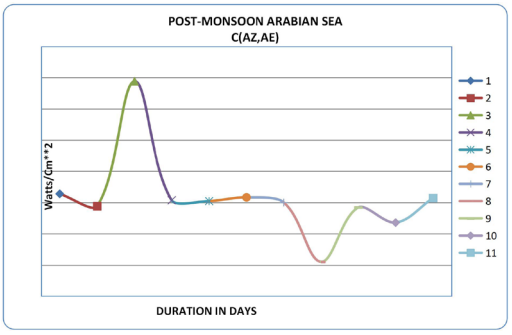

Figure 12 (a). Daily mean of C(Az,Ae) case wise – post monsoon: Arabian Sea

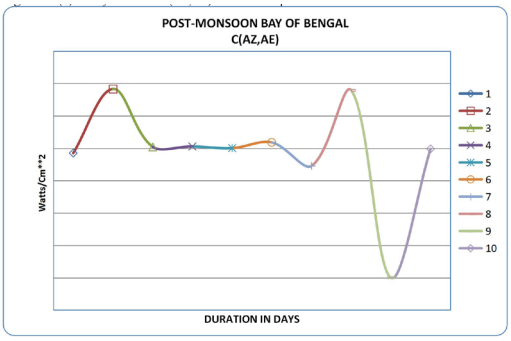

Figure 12 (b). Daily mean of C(Az,Ae) case wise – post monsoon: Bay of Bengal

4. Conclusions

Based on the frequency/ trend analysis of cyclones over the period from 1991 to 2013 following may be concluded:

1) The maximum frequency of formation of cyclones over BOB is twice that over AS. Further, it is noticed that over BOB they are more frequently formed in the post monsoon season compared to pre monsoon season.

2) The overall trend for both basins is of just decreasing type in both seasons. The decreasing trend being more evident in the post monsoon season in case of the AS and in the case of BOB it is more evident in the pre monsoon season.

Based on the computation of various energetic terms and subsequent comparison of the energy conversion terms following may be concluded:

3) In both the seasons, Ae was generated at the cost of Ke on a daily scale in the formative and mature stage of cyclones under study which resulted into their intensification. The same may be attributed to contour trough lagging behind the thermal trough. In the dissipating stage the enhancement of Ke indicates cyclones gained movement in this stage. In both the basins the above pattern was observed, however, certain cyclones over BOB gained movement from the formative stage itself and continued gaining movement till the end of their life-cycle. This is indicative that thermally directed circulation was strong for these cyclones over the entire period.

4) In both the basins, at the time of cyclone intensification; Az is generated at the cost of Kz during pre monsoon. This may be attributed to weakened mean meridional circulation in both basins during the pre monsoon season. However, during post monsoon the continual generation of Kz at the cost of Az of some cyclones may be attributed to strong mean meridional circulation over the systems during that time.

5) In both the basins, the enhancement of Ke and generation of maximum wind speed at the expense of Kz during pre monsoon and post monsoon was during the formative and mature stage. This, along with generation of Ke from Ae for the same period suggests an enhancement of Ke which may be attributed to the enhancement in both the barotropic and baroclinic conversion into Ke. Although there were some cyclones (over both basins) that developed in the post monsoon, which showed a departure from this pattern and had maximum wind speed which was generated at the cost of Kz only during the dissipating stage. It is to be noted that the enhancement in Kz from Az was observed continually over some cyclones in post monsoon. This shows that the energy flow here was Az -> Kz -> Ke.

6) In both the basins, the mid latitude baroclinic circulation might have influenced significantly on the development and intensification of the selected cyclones. However, during dissipation there was hardly any influence of mid latitude baroclinic circulation.

Acknowledgement: NCEP Daily Global Analyses data provided by the NOAA/OAR/ESRL PSD, Boulder, Colorado, USA, from their Web site at http://www.esrl.noaa.gov/psd/. The authors gratefully acknowledge DGM, IMD, and Director, IITM for providing the facilities in carrying out this study.

References

[1] Akter N. and Tsuboki K., 2014, "Role of synoptic-scale forcing in cyclogenesis over the Bay of Bengal, Climat Dynamics, 43:2651-2662. DOI 10.1007/s00382-014-2077-9.

[2] Devi, Sunitha S, Dutta, Somenath and Prasad, K , 2014, "Energetics of Super cyclone 'Gonu' and Very Severe Cyclonic Strom 'SIDR'", Mausam, 65:37-48.

[3] Dutta, Somenath, Narkhedkar, S.G., Sikka, D.R. and Devi, S., (2011), "A Dynamical Comparison between two recent drought southwest monsoon seasons 2002 and 2009 over India", Mausam, 62:133-144.

[4] Dutta, Somenath, Narkhedkar S.G., Devi, S, Sikka, D.R.,(2012),"A composite energetics study for contrasting south west monsoon years in the recent decade", Atmósfera 25:109-126.

[5] ESCAP-WMO Panel on Tropical Cyclone Feb, (2013), "The 40th session of the Panel on Tropical Cyclones, Colombo, Sri Lanka from 25 February to 1 March 2013".

[6] Joint Typhoon Warning Center (JTWC), (1974), "Annual Typhoon Report". U.S. Fleet

DOI: https://doi.org/10.30564/jasr.v2i1.266

[7] Weather Central, Joint Typhoon Warning Center, COMNAVMARIANAS, Box 17, FPO San Francisco, CA, 96630, U.S., 116 pp.

[8] Karl, Hoarau, Ludovic, Chalogne, (2010), "A climatology of the intense tropical cyclones over the past three decades from 1990-2008", Accepted as a chapter for: "Indian Ocean Tropical Cyclones and Climate Change", Part 1, pp 3-7, published by Springer Netherlands.

[9] Holton, James R., (2004), "An Introduction to Dynamic Meteorology", Volume 1, published by Academic Press.

[10] Keshavamurty R.N. and S. T. Awade, (1970), "On the maintenance of the mean monsoon trough over north India", Mon. Wea. Rev. 98: 315-320.

[11] Krishnamurti T. N. and Ramanathan Y., (1982), "Sensitivity of monsoon onset of differential Heating". J. Atmos. Sci. 39:1290-1306.

[12] Krishnamurti T. N., (1985), "Summer monsoon experiment-A review". Mon. Wea. Rev. 113: 1590-1626.

[13] Krishnamurti T.N. and N. Surgi, (1987), "Observational aspects of summer monsoon, Monsoon Meteorology", Edited by C.P. Chang and T. N. Krishnamurti, Oxford University press, 3-25.

[14] Krishnamurti, T.N and Bounoua, L, (2000), "An Introduction to Numerical Weather Prediction Techniques", CRC press Inc, pp. 1-286.

[15] Krishnamurti T. N., Martin A., Krishnamurti R., Simon A, Thomas A., Vinay Kumar (2013), "Impacts of enhanced CCN on the organization of convection and recent reduced counts of monsoon depressions", Climate Dynamics, 41:117–134.

[16] Landsea, C. W., (1993), "A climatology of intense (or major) Atlantic hurricanes. Mon. Wea. Rev., 121:1703-1713.

[17] Landsea, C. W., (1997a), Comments on "Will greenhouse gas-induced warming over the next 50 years lead to higher frequency and greater internsity of hurricanes?", Tellus, 49A: 622-623.

[18] Landsea, C. W., (2000), "El Niño-Southern Oscillation and the seasonal predictability of tropical cyclones". Accepted as a chapter for El Ni*ño* and Southern Oscillation : "Multiscale Variability and Global and Regional Impacts", edited by H. F. Diaz and V. Markgraf :149-181.

[19] Munshi, Jamal, (2015), "Tropical Cyclones in the Indian Ocean 1998-2014", uploaded in the Social Science Research Network, pp. 9

[20] Neumann, C. J., (1993), Global Overview, "Global Guide to Tropical Cyclone Forecasting", WMO/TC-No. 560, Report No. TCP-31, World Meteorological Organization, Geneva, 1-1 - 1-43

[21] Raju P. V. S., U. C. Mohanty and R. Batla, (2002), "The contrasting features of the Asian summer monsoon during surplus and deficient rainfall over India". International journal of climatology, 22:1897-1914.

[22] Rao K.V. and S. Rajamani, (1972), "Study of heat sources and sinks and the generation of available potential energy in the Indian region during Southwest monsoon". Mon. Wea. Rev, 100:383-388.

[23] Rao P. L. S., (2006), "The kinetic energy budget of Asian summer monson", Theoretical and Applied Climatology, 84:191-205.

[24] Rao P. L. S. and U. C. Mohanty, (2007), "Temporal characteristics of the Indian southwest Monsoon". Natural hazards, 42:335-344.

[25] Yanai M., C. F. Li and Z, S, Song, (1992), "Seasonal heating of the Tibetan Plateau and its effects on the evolution of the Asian Summer monsoon". J. Meteor. Soc. Jap., 70:319-351.

 DOI: https://doi.org/10.30564/jasr.v2i1.266

BILINGUAL PUBLISHING CO.
Pioneer of Global Academics Since 1984

Journal of Atmospheric Science Research
http://ojs.bilpublishing.com/index.php/jasr

ARTICLE

Moderate Geomagnetic Storm Condition, WAAS Alerts and Real GPS Positioning Quality

Vladislav V. Demyanov[1*] Xinggang Zhang[2*] Xiaochun Lu[2]

1 Irkutsk State Transport University, 664074 Chernyshevskogo str.15, Irkutsk, Russia
2 National Time Service Center, Shuyuan east Road 3, Lintong District, Xi'An, China

ARTICLE INFO

Article history
Received: 22 November 2018
Accepted: 7 January 2019
Published: 1 March 2019

Keywords:
Ionosphere and SBAS
Auroral oval and WAAS integrity
DGPS
Differential GNSS integrity under geomagnetic storms

ABSTRACT

The most significant part of Wade Area Augmentation System (WAAS) integrity consists of the User Differential Range Error (UDRE) and the Grid Ionospheric Vertical Error (GIVE). WAAS solutions are not completely appropriate to determine the GIVE term within the entire coverage zone taking in account real irregular structure of the ionosphere. It leads to the larger confidence bounding terms and lower expected positioning availability in comparison to the reality under geomagnetic storm conditions and system outages. Thus a question arises: is the basic WAAS concept appropriate to provide the same efficiency of the integrity monitoring for both "global differential correction" (i.e. clock, ephemeris et al.) and "local differential correction" (i.e. ionosphrere, troposhpere and multipath)? The aim of this paper is to compare official WAAS integrity monitoring reports and real positioning quality in US coverage zone (CONUS) and Canada area under geomagnetic storm con-ditions and system outages. In this research we are interested in compari-son between real GPS positioning quality based on single-frequency C/A ranging mode and HAL (VAL) values which correspond to the LP, LPV and LPV200 requirements. Significant mismatch of the information be-tween WAAS integrity data and real positioning quality was unfolded as a result of this comparison under geomagnetic storms and system outages on February 14, 2011 and June 22, 2015. Based on this result we think that in order to achieve high confidence of WAAS positioning availability alerts real ionospheric measurements within the wide area coverage zone must be involved instead of the WAAS GIVE values. The better way to realize this idea is to combine WAAS solutions to derive "global differential cor-rections" and LAAS solutions to derive "local differential corrections".

1. Introduction

The Wide Area Augmentation System (WAAS) provides not only differential corrections, but also ranging error associated confidence bounds to ensure the integrity of the positioning service throughout the United States and Canada. The WAAS Master Station calculates integrity data associated with its generated corrections at the required level of integrity for the intended flight operation. Integrity data is provided in the form of rang-

**Corresponding Author:*
Vladislav V. Demyanov; Irkutsk State Transport University, 664074 Chernyshevskogo str.15, Irkutsk, Russia
Email: vv.emyanov@gmail.com
Xinggang Zhang; National Time Service Center, Shuyuan east Road 3, Lintong District, Xi'An, China
Email: zxg@ntsc.ac.cn

 DOI: https://doi.org/10.30564/jasr.v2i1.343

ing error confident bounds which are broadcast within WAAS coverage zone and is used in order to compute the protection levels (PL) taking into account both all relevant ranging error sources and local "satellite-user" geometry. Depending on the flight operation, the user equipment may either compute a Horizontal Protection Level (HPL) or both a HPL and a Vertical Protection Level (VPL). WAAS guarantees that the user's actual position error will be smaller than PL values during 99.99999% of the time. The following level accuracy and availability for the WAAS coverage zone has been accepted as:

1) Localizer Performance (LP) service is available when the calculated HPL is less than 40 meters;

2) Localizer Performance with Vertical Guidance (LPV) service is available when the calculated HPL is less than 40 meters and the VPL is less than 50 meters;

3) Localizer Performance with Vertical Guidance to 200 foot decision height (LPV200) service is available when the calculated HPL is less than 40 meters and the VPL is less than 35 meters.

The receiver user compares the computed protection levels with the alert limit (AL) thresholds established for the horizontal plane (HAL) and the vertical plane (VAL) for a selected phase of flight. If one of the protection levels exceeds the corresponding alert limit, the receiver provides an annunciation to the user [1].

The most significant part of the integrity data consists of the User Differential Range Error (UDRE) and the Grid Ionospheric Vertical Error (GIVE). The UDRE characterizes the residual error in the fast and long term "global" corrections of both ephemeris and reference oscillator associated errors. The UDRE is broadcast by the WAAS for each satellite that is monitored by the system and the 99.9% bound (3.29 sigma) of the residual error on a pseudo range after application of fast and long-term cor-rections is checked. The GIVE characterizes the residual error in the current ionospheric correction (IC), for the estimated ionosphere signal vertical delays are calculat-ed for each of WAAS ionospheric grid point (IGPs) and broadcasted every 5 minutes [1]. Since the true ionospheric delay and multipath error are not precisely known, the estimated variants in these error sources are added to the UDRE, before comparing it to the residual error [2].

It is obvious that reliability of WAAS service integrity depends on how the UDRE and GIVE confidence bounds correspond to the real positioning environment. It is well known that current availability of WAAS service strictly depends on both the quality of each individual satellite vehicle (SV) ranging and SVs constellation geometry at the user's location. Positioning delusion of precision (PDOP) describes local "satellite-user" geometry and it is unique and unpredictable for each particular user within the WAAS coverage zone. Hence the confidence bounds are established according to the expected UDRE and GIVE values.

For the WAAS, ionospheric ranging errors are the most significant and unpredictable. The horizontal and, especially, the vertical positioning availability are easily to be disturbed in the ionosphere [3]. At mid-latitudes such disturbances mostly appear during the main phase of geomagnetic storms and can cause both increasing ranging error and some short outages of GPS SVs [4,5,6]. Nevertheless a user derives the GIVE value anywhere in the coverage zone based on the interpolation solutions from the nearest WAAS ionospheric grid points (IGPs) data to compute individual protection levels. In our opin-ion such a method of the ionospheric signal delays data treatment to get GIVE confidence bounds is not able to deal with undetected multi-scale ionospheric disturbanc-es and yields high probability of false alarm of the HAL (VAL) exceeding. As WAAS solutions are disable to de-termine the GIVE term within the entire coverage zone taking in to account the real irregular structure of the ionosphere it leads larger confidence bounding terms and lower expected positioning availability in comparison to the reality under geomagnetic storm conditions.

The aim of this paper is to compare official WAAS integrity monitoring reports [www.nstb.tc.faa.gov/DisplayDailyPlotArchive.htm] and real positioning quality in US coverage zone (CONUS) and Canada under geomagnetic storm conditions and system outages. In this paper we are interested in the comparison between real GPS positioning quality based on single-frequency C/A mode and HAL (VAL) values which corre-spond to the LP, LPV and LPV200 requirements. The aim of such research is to make a first step to answer the question: "Can we use the WAAS typical solutions to provide LPV and LPV200 service outages alerts with required confidence taking in to account the real environment for the future GNSS SBAS?"

2. Data Sources and Experimental Environment

We conducted our research under geomagnetic storms condition on February 14-15, 2011 and June 22-23, 2015. Table 1 collects these storms parameters based on geomagnetic data from [https://cdaweb.sci.gsfc.nasa.gov/]. The main parameters of geomagnetic storm such as the time of sadden commencement (Tssc), periods of the initial phase (IP), the main phase (MP) and the re-

DOI: https://doi.org/10.30564/jasr.v2i1.343

covering phase (RP) as well as the variations of the horizontal component of the geomagnetic field (Ht) were derived from the high-latitude ground-based magnetometer data at Hampton, Alaska (Lat 64.9, Long 212.1) [https://cdaweb.sci.gsfc.nasa.gov/cgi-bin/eval1.cgi].

Comparison of the above mentioned geomagnetic events displays that the February 14-15, 2015 event has short MP period, weak geomagnetic, hence, ionospheric disturbances and can be considered as a moderate geomagnetic storm. In contrast to that the June 22-23, 2015 event is a strong geomagnetic storm which has a long MP period and should be accompanied with significant ionospheric disturbances and can bring significant impact on WAAS and GNSS performance.

Table 1. The geomagnetic storms characteristics

Date (yy-mm-dd)	3-hour Kpmax	TSSC, UTC	IP period	MP period	RP period	Htmin, nT	Htmin - Htmax, nT
2011-02-14	4	16.00	16.00-20.30	20.30-23.30	After 23.30	12420	12420-12830
2015-06-22	8	05.30	05.30-12.30	12.30-20.00	After 20.00	11500	11500-13000

Usually weak geomagnetic storm is unlikely to induce strong ionospheric disturbances into the mid-latitudes ionosphere. As it was found earlier [7] the multiscale ionospheric disturbances propagates toward the mid-latitudes from the expanding south boarder of the auroral oval which is considered as a source of acoustic-gravity waves. The area of the auroral oval boarder expands as the further the stronger geomagnetic storm is. So it is unlikely that a weak geomagnetic storm on February 14-15, 2011 is able to inspire strong travelling ionospheric disturbances toward the mid-latitudes. There for the real ionosphere shall not be significantly disturbed in mid-latitudes and the expected WAAS area coverage zone should not shrink as a result of the ionospheric disturbances than.

On the other hand, strong geomagnetic storm, like the event on June 22-23, 2015, can bring serious WAAS performance deterioration. Thus it would be interesting to compare the official WAAS alerts and real GPS positioning quality under both weak and strong geomagnetic storm conditions. That was the reason why we choose the above mentioned days for our research in this paper.

The WAAS official data source [http://www.nstb.tc.faa.gov/DisplayDailyPlotArchive.htm] issued alert reports for the CONUS zone. Fig. 1 a,b displays percent of CONUS area covered with LP, LPV and LPV2000 services versus Greenwech Mean Time (GMT) time on February14 (panel b) and 15 (panel a), 2011.

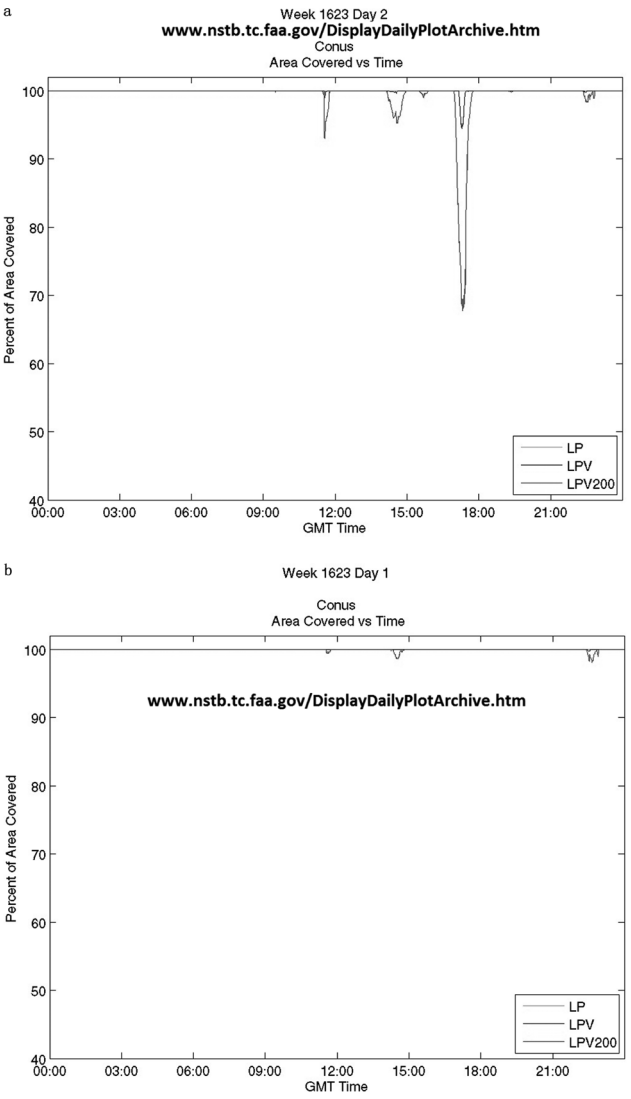

Figure 1. Percent of CONUS area covered vs GMT for the day of the main phase of geomagnetic storm on Feb.14, 2011(panel b) and for the day of recovering phase of the geomagnetic storm on Feb 15, 2011 (panel a)

Regardless the main phase of the geomagnetic storm that took place on February14, 2011, we can see that there is no significant coverage zone shrinking for LP, LPV and LPV200 service on this day. However we have WAAS alert of sharp shrinking of the coverage zone at about 17.40 GMT on February 15, 2011 for LPV200 service. This time period corresponds to the end of the recovering phase of the geomagnetic storm. Thereby the ionospheric disturbances are not the probable source of the WAAS coverage zone shrinking here.

Figure 2 displays daily WAAS CONUS LPV and LPV200 coverage versus date and daily Kp indices for a period from January 1st till April 1st 2011 [8]. One can see that sharp shrinking of the WAAS CONUS coverage zone for LPV and LPV200 took place on February 15, 2011 as

 DOI: https://doi.org/10.30564/jasr.v2i1.343

well. WAAS CONUS LPV and LPV200 percent of area covered is reduced down to 89% and 73% correspondently.

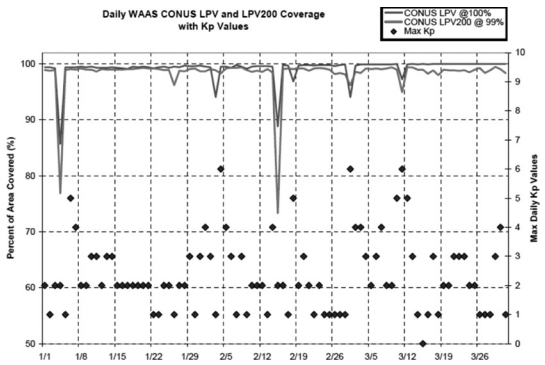

Figure 2. Daily percent of CONUS WAAS area coverage and Kp values versus time[8]

The WAAS service degradation can be caused by not only the ionosphere impact but also by the WAAS and GPS segments outages. Table 2 contains a list of the system outages which took place on February 14 and 15 2011 [8]. According to the Table there was GEO Uplink Subsystem (GUS) event for the geostationary satellite GEO138 on February 14, 2011. This event did not cause the LPV and LPV200 outages on this day thanks to the other GEOs, which were used to broadcast WAAS corrections.

There was a long outage for GPS SV PRN 21 (from 11.15 till 20.05 GMT) and short outage for GPS SV PRN 4 (from 11.32 till 11.43 GMT). It means that there were two GPS SV out of service within the period from 11.32 till 11.43 concurrently. These events do not have time coincidence with the WAAS alert picture (Fig. 1) for whole CONUS zone, but according to the WAAS forecast these outages brought LPV and LPV200 service outage in California, the USA North-Central, Arizona and Florida on February 15, 2011.

Fig. 3 a,b displays percent of Canadian area covered with LP, LPV and LPV2000 services vs GMT on June 20 (panel a) and June 22 (panel b), 2015 [http://www.nstb.tc.faa.gov/DisplayDailyPlotArchive.htm].

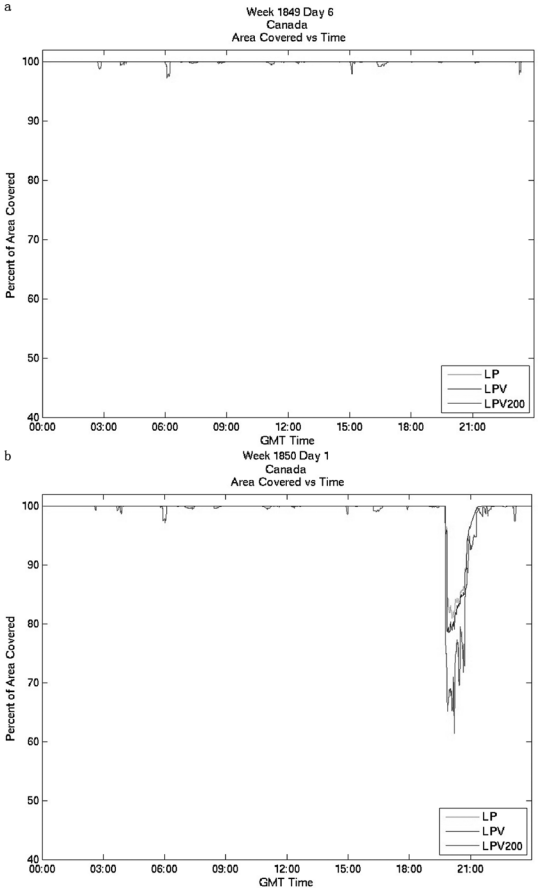

Figure 3. Percent of Canadian area covered vs GMT for the day of the geomagnetic storm on June 22, 2015 (panel b) and for the background day on June 20, 2015 (panel a)

Based on the Fig 3, we can see that there was significant degradation of all the LP, LPV and LPV-200 services coverage in Canada from about 19:30 GMT till 21:30 GMT on June 22nd. This time period corresponds to the main phase of strong geomagnetic storm (see Table 1). Fig 4 displays an apparent time coincidence between high Kp=8 and sharp deterioration of LPV and LPV200 services coverage in Canada on June 22, 2015 as well [9].

Table 2. WAAS and GPS events on February 14 and 15, 2011

Start Date	End Date	Location/ Satellite	Service Affected	Event Description
02/14/11	02/14/11	GEO138, Woodbine (QWE)	All	GUS switchover, Woodbine faulted. TOW 127889-127902
02/15/11	02/15/11	PRN21	All	NANU 2011015. There was a NANU 2011015 on PRN 21 from 11:15am to 20:05pm GMT and SV Alert on PRN 4 (11:32am-11:43am), which both affected LPV and LPV200 coverage; W1623D2 LPV Outages: 1. California outage due to SV alert on PRN 4; 2. North-Central and Arizona outages due to NANU on PRN 21 LPV200 Outages: 1. California outage due to SV alert on PRN 4; 2. North-Central, Arizona and Florida outages due to NANU on PRN 21;

DOI: https://doi.org/10.30564/jasr.v2i1.343

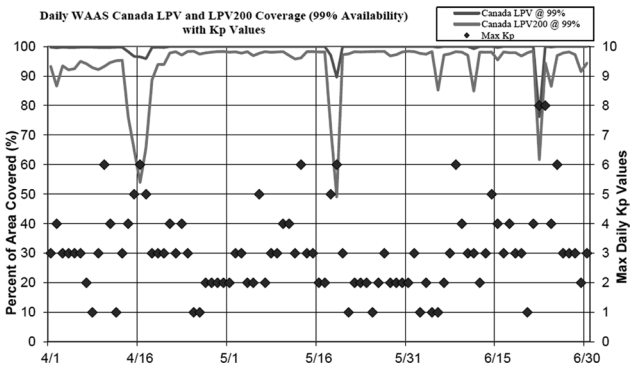

Figure 4. Daily percent of Canada LPV and LPV200 service area coverage and Kp values versus time

Table 3 contents the LPV (LPV200) service degradation event description. In contrast to the previous case (see Table 2) the service degradation for all the North America coverage zone is caused by the ionospheric disturbances as a result of strong geomagnetic storm on June 22-23, 2015 [9].

According to Table 3 there were no GPS/WAAS segment outages during the event on June 22, 2015 so we can be sure that the LPV and LPV200 service degradation was caused with elevated GIVE values as a result of the ionospheric geomagnetic disturbances. As all the events took place during the MP and the beginning of the RP of the geomagnetic storm we can probably consider the LPV and the LPV200 service degradation as a result of the travelling ionospheric disturbances from the pulsing auroral oval border [7].

3. Data Sources and Data Treatment

To compare the WAAS alerts to the real positioning quality we utilized RINEX 2.0 data files with 30-s time resolution which are available on [http://lox.ucsd.edu/pub/rinex/]. These data corresponds to GPS-sites which are placed in CONUS and Canada zones. For our research goals 70 sites in CONUS zone (excluding California) and 30 sites in Canada were chosen. The CONUS sites were equipped with the same GPS receiver type Trimble in order to avoid influence of the apparatus features of different GPS receiver type to our final results. Unfortunately there were not enough sites equipped with the same type of receivers in Canada. These Canadian sites were equipped with different types of receivers such as TPS Net, Leica, Ashtech, Trimble, AOA and Turbo-Rogue. The map of these sites location for both CONUS and Canada zones is displayed in Fig.5.

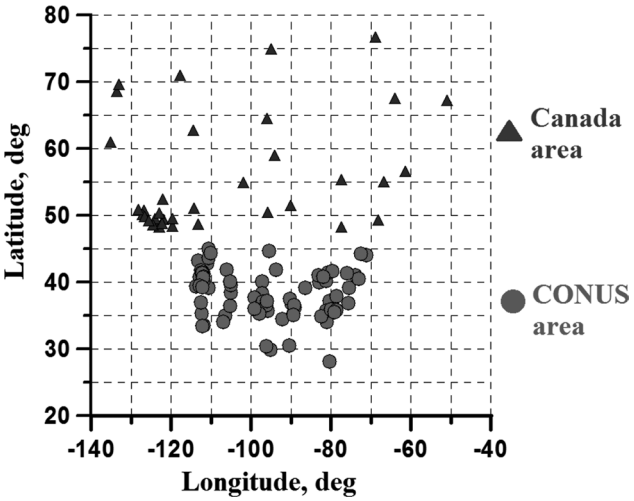

Figure 5. A map of the GPS-sites location within CONUS and Canada zone coverage zone

Firstly, it is interesting to compare the WAAS alert figures (Fig1-4) and the real positioning quality in CONUS and Canada coverage zone. In order to do this a percent of area coverage with the real positioning service for CONUS and Canada zones was derived, based on the RINEX data for each of GPS-sites (Fig 5) in one-frequency with the GPS standalone mode. TEQC software [10] was utilized to get navigation solutions and the correspondent positioning errors for the GPS-sites. Doing this, we did not use the ionospheric correction and GPS SV outages report (Table 2) in order to simulate that GPS standalone mode which

Table 3. WAAS and GPS events on June 22, 2015

Start Date	End Date	Location/ Satellite	Service Affected	Event Description
2016/06/22	2016/06/23	Washington D.C. (CnV), Los Angeles (CnV), Atlanta (CnV)	LPV_All, LPV200_All,	Geomagnetic activity (Kp = 8) disturbed the ionosphere causing elevated GIVE values. This resulted in significant degradation of: (1) LPV-200 service coverage in Canada from about 19:45 GMT until 21:35 GMT on June 22nd. The elevated GIVE values also resulted in moderate degradation of: (1) LPV service coverage in Canada from about 19:45 to 21:16 GMT on June 22nd; (2) LPV-200 service coverage in CONUS (Northeast) from about 19:45 to 21:07 GMT on June 22nd. The elevated GIVE values also resulted in minor degradation of: (1) LPV service coverage in CONUS (Northeast) from about 19:45 to 20:45 GMT on June 22nd and LPV-200 service coverage in Alaska from about 20:16 to 20:26 GMT on June 22nd

 DOI: https://doi.org/10.30564/jasr.v2i1.343

corresponds to the worst case of positioning conditions.

In case of mismatch of alert figures from the WAAS output and TEQC output we need to involve another independent solution for HPL (VAL) computation to decide which alert corresponds to the real environment better. In order to do it, we compute HPL (VAL) values based on the real ionospheric ranging error statistics, instead of GIVE values for each GPS site within CONUS and Canada zones. Taking all of this in to account, our strategy of the data treatment includes following steps:

1) Getting the navigation solutions with 30-s time resolution for each GPS site (Fig.5) utilizing RINEX within one-frequency C/A ranging data and TEQC software. Once the navigation solution had been received we computed the positioning errors of each GPS site and transform the error values from rectangular Earth-centered coordinate system to the local coordinate system;

2) Comparison between the LP, LPV and LPV200 alarm limits (HAL and VAL) and real positioning errors which were computed at the pervious step. Every time when positioning error exceeds correspondent alarm limit a positioning fault is fixed for the GPS site according to LP, LPV or LPV200 limits particularly. Finally the real percent of the area covered for CONUS or Canada zone is computed as following:

$$\%\,\text{of}\quad \text{Area}\quad \text{covered} = \frac{(N_{TOT} - N_{FLT})}{N_{TOT}} \cdot 100\% \quad (1)$$

Where N_{TOT} is total amount of GPS-sites within the area under consideration; N_{FLT} is the number of the GPS-sites where the current positioning errors exceed either the VAL or HAL values according to the LP, LPV or LPV200 services.

3) A computation current HPL and VPL values taking in to account the real ionospheric ranging errors instead of correspondent GIVE values. In order to do this, a "model ranging" and real SVs constellation were utilized for each GPS-site within the CONUS or Canada zone. Here we define "model ranging" as following:

$$\begin{aligned}
&\rho_i = R_{GEOM,i} + \Delta R_{ion,i} \\
&R_{GEOM,i} = \sqrt{\left(x_{0,i} - x_{US}\right)^2 + \left(y_{0,i} - y_{US}\right)^2 + \left(z_{0,i} - z_{US}\right)^2} \\
&\Delta R_{ion,i} = \frac{40.308}{f_1^2} \cdot TEC_i \\
&TEC_i = \frac{1}{40.308} \cdot \frac{f_1^2 \cdot f_2^2}{f_1^2 - f_2^2} \cdot \left(C1_i - P2_i\right)
\end{aligned} \quad (2)$$

Where: $x_{0,i}, y_{0,i}, z_{0,i}$ and x_{US}, y_{US}, z_{US} are i-th SV position and user's position in the rectangular Earth-centered coordinate system. These data can be found or computed from the correspondent RINEX files; TEC_i is ionospheric total electron content along the "*i*-th SV-user" line-of-site (in TECU, 1TECU=10^{16} 1/m^2); f_1=1575.25 GHz and f_2= 1227.75 GHz are the GPS operation frequencies; $C1_i$ is C/A-code ranging at frequency f_1 and $P2_i$ is P-code ranging at frequency f_2 which can be derived from RINEX observation file for each SV in view.

Computation of the HPL and VPL protection levels for a "model ranging" (2) and the real SVs constellation for each of the GPS-sites can be done as following [11]

$$\begin{aligned}
&HPL = \begin{cases} K_{HNPA} \cdot D_{mjr} \\ \text{or} \\ K_{HPA} \cdot D_{mjr} \end{cases}; \quad VPL = K_{VPA} \cdot D_V \\
&D_{mjr} = \sqrt{\frac{D_X^2 + D_Y^2}{2} + \sqrt{\left(\frac{D_X^2 - D_Y^2}{2}\right)^2 + D_{XY}^2}} \\
&D_X^2 = \sum_{i=1}^{N} S_{X,i}^2 \cdot \sigma_i^2; \quad D_Y^2 = \sum_{i=1}^{N} S_{Y,i}^2 \cdot \sigma_i^2; \quad D_V^2 = \sum_{i=1}^{N} S_{V,i}^2 \cdot \sigma_i^2 \\
&D_{XY} = \sum_{i=1}^{N} S_{X,i} \cdot S_{Y,i} \cdot \sigma_i^2 \\
&\mathbf{S} = \begin{vmatrix} S_{X,1} & S_{X,2} & \ldots\ldots & S_{X,N} \\ S_{Y,1} & S_{Y,2} & \ldots\ldots & S_{Y,N} \\ S_{V,1} & S_{V,2} & \ldots\ldots & S_{V,N} \\ S_{t,1} & S_{t,2} & \ldots\ldots & S_{t,N} \end{vmatrix} = \left(\mathbf{G}^T \cdot \mathbf{W} \cdot \mathbf{G}\right)^{-1} \cdot \mathbf{G}^T \cdot \mathbf{W}
\end{aligned} \quad (3)$$

Where K_{HNPA}=6.18 is a coefficient of confidence bounds in horizontal plane for non-precise landing approaching; K_{HPA}=6.0 is a coefficient of confidence bounds in horizontal plane for precise landing approaching with vertical guidance; K_{VPA}=5.33 is a coefficient of confidence bounds in vertical plane for a precise landing approach with vertical guidance; G is current "SV-user" angular geometry matrix; W is diagonal ranging errors weighting matrix; σ_i is a standard deviation of the "model ranging" error (2) for *i*-th SV.

As we need to find σ_i – values for each SV in the view before the HPL and VPL computation it means that we have to accumulate simultaneous ranging values within some time interval. The time interval of ΔT= 5 min was used in our computation here.

4) A comparison between the current HPL and VPL values (3) and correspondent alarm levels of LP, LPV and LPV200 services for each GPS-site from CONUS or Canada areas and the percent of area covered computation (1) than.

To model the ranging time series (2) based on the real data from the correspondent RINEX files the double-frequency P1 (or C1) - P2 "code-code" combination was utilized. It means that the current $\Delta R_{ion,i}$ value (2) contents not only the pure ionospheric signal delays but also the residuals of all the frequency dependent ranging errors, such as multipath error and differential code biases (DCB)

DOI: https://doi.org/10.30564/jasr.v2i1.343

in SV and the receiver equipment.

In order to understand the final results clearly we should evaluate expected ranging errors before getting navigation solution from the "model ranging" data. Based on a long time research it has been accepted that the most probable value of the vertical user ionospheric range error (UIRE) can be assumed in the WAAS solutions as follows [11]

$$\Delta R_{UIRE,V} = \begin{cases} 9.0\,m & 0^\circ \le \phi_{PP} \le 20^\circ \\ 4.5\,m & 20^\circ < \phi_{PP} \le 55^\circ \\ 6.0\,m & 55^\circ < \phi_{PP} \end{cases} \quad (4)$$

Where φ_{PP} is the latitude of the ionospheric pierce point.

To transform this vertical range error into the correspondent slant error value we can use following equation [12]

$$\Delta R_{UIRE,SLT} = \Delta R_{UIRE,V} \cdot \left(1 - \left(\frac{R_E \cos(ELE)}{R_E + h_{F2}}\right)^2\right)^{-0.5} \quad (5)$$

Where R_E =6378.1363 km is the Earth radius; h_{F2}=350 km is the height of the F2 layer electronic density maximum concentration; ELE is a SV elevation angle.

Based on the IGS statistics of the expected ionospheric TEC grid forecasting the 1-sigma confidence bounds of this parameter should be within 2-9 TECU (correspondent UIRE is from 0.32 to 1.44 m).

The absolute value of standard mean of the SV DCB shall not exceed 15 ns (4.5 m). The main DCB can be either positive or negative. The random variations of this value shall not exceed 3 ns i.e. 0.9 m (two sigma). In a reality SV DCB differs significantly for different types of SV and can vary within +/- 12 ns (i.e. +/- 3.6 m) from one SV to another. SV DCB value has a long lasting trend changing as much as 0.3-0.5 ns per year [13,14].

DCB values for the GPS receiver strictly depends on the receiver type and environment condition. According to [14] it was found that, the absolute value of receiver DCB can vary within +/- 40 ns (i.e +/-12 m) for the Trimble 5700 and Trimble NETP types. The random variations of this value (1-sigma) shall not exceed 2 ns (0.6 m). Like the previous item, the mean of this code delay can be either positive or negative and have the long annual trend.

There are many evaluations of multiphase effects on the GNSS performance [15,16]. This error is usually considered as zero-mean Gaussian noise with standard deviation which depends on the SV elevation angle as following [11].

$$\sigma_{MPH} = 0.13 + 0.53 \cdot \exp\left(\frac{-ELE_i}{10^{\mathrm{O}}}\right) \quad (6)$$

Based on (6) the one-sigma confidence bound of multipath error standard deviation is within 0.13 – 0.4 m depending on the SV elevation angle.

Taking into account all the above mentioned components we can expect that standard mean of the $\Delta R_{ion,i}$ values (2) which were derived from the RINEX (P1(C1)-P2) data is expected to be from -3.2 to 28 m and correspondent standard deviation is from 0.8 to 4.2 m. Figure 6 displays daily values of standard mean and standard deviation of $\Delta R_{ion,i}$ values which were derived from RINEX data utilizing (2) for each GPS-site in CONUS area. One can see that all these values are within the previously computed borders. There is no significant difference between these data on February 14 and 15, 2011. Figure 7 displays the same data which were derived from RINEX data for each GPS-site in Canada.

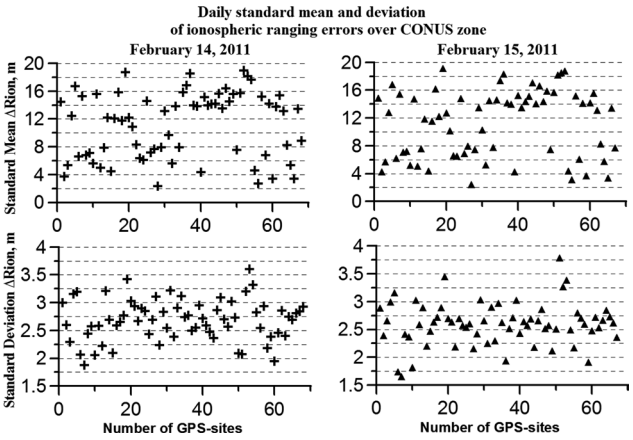

Figure 6. Daily Standard Mean and Standard Deviation of the ionospheric ranging errors derived from the RINEX data corresponding to the GPS sites which are within CONUS zone on February 14 (left panel) and February 15 (right panel), 2011

Two groups of the daily standard mean of $\Delta R_{ion,i}$ values can be recognized in Fig 6 according to their values. First group of the standard mean values lies within 10-20 meters but another group is within 2-10 m. This difference probably can be explained with different type of antennas and GPS receivers which are set on different GPS-sites under our consideration. On the other hand there is no such a significant difference between standard deviation values which were taken from the same data series. All the values vary within the 1.5-3.7 m on both February 14 and 15, 2011.

Regardless the Canadian GPS-network contain the GPS receivers of several types, similar features of the daily standard mean and standard deviation can be seen in

 DOI: https://doi.org/10.30564/jasr.v2i1.343

Fig.7. Most of the daily standard mean of $\Delta R_{ion,i}$ values lie within 2-10 m. On the other hand a bit higher standard deviation values can be seen here. All the values vary within the 1.6-4.2 m on both June 20th and 22nd, 2015.

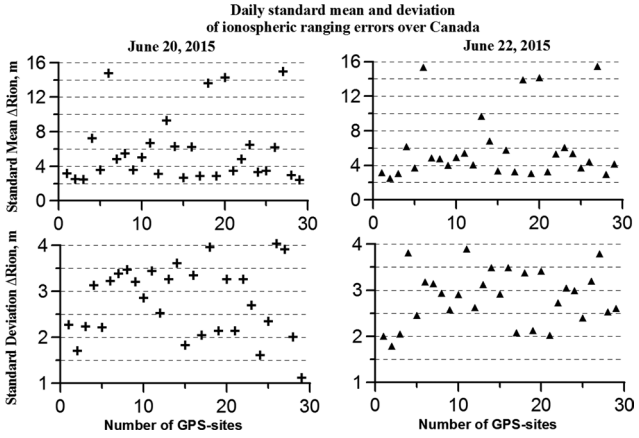

Figure 7. Daily Standard Mean and Standard Deviation of the ionospheric ranging errors derived from the RINEX data corresponding to the GPS sites which are within Canada on June 20th (left panel) and June 22nd (right panel), 2015

3.1 Real Positioning Quality and WAAS Alerts Comparison

Positioning quality is considered at the standpoint of the protection cylinder concept[1]. This protection cylinder, is centered on the user's calculated position and represents the uncertainty of the position according to user's true position at each time point. In our research the data from the GPS-sites with constant position is used. Thus user's true position can be considered as known. On the other hand the alert limit cylinder is utilized to check if the current positioning accuracy corresponds to LP, LPV or LPV200 required positioning accuracy. The alert limit cylinder is centered on the user's calculated position, just as the protection level cylinder, and defined with the HAL and VAL borders. In case if the user's calculated positioning errors exceeds either the VAL or HAL values, it means that required positioning accuracy is not available.

The percent of area covered (1) was computed for the LP, LPV and LPV200 alert limits particularly. To evaluate positioning quality from TEQC output data we did not use any ionospheric correction in order to pure the prob-able ionospheric impact better. Fig.8 displays the percent of CONUS area covered versus UT. Can be seen that the percent of area covered was not decreasing lower than 82% for all protection limits neither on February 14th (the main phase of geomagnetic storm) nor on February 15th (recovering phase of geomagnetic storm).

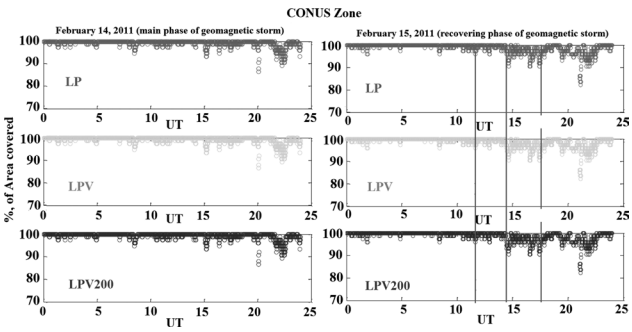

Figure 8. TEQC output: percent of CONUS area covered vs Time on Feb. 14 (left panel) and on Feb. 15 (right panel), 2011. Red lines mark approximate time points which correspond to WAAS alerts (see Fig 1a).

Comparison between these results and the WAAS official alerts (Fig.1,2) displays following:

1) TEQC output data analysis displays that positioning quality is worse within the time period from 15.00 to 23.00 UT on February 15 in comparison to the same time on the previous day. This time period corresponds to the end of recovering phase of the geomagnetic storm (Table 1). Hence the percent of area coverage shrinking is not likely caused with the ionospheric geomagnetic disturbances in this time period. According to Table 2, there was a long SV PRN 21 outage from 11.15 till 20.05 UT, so it can be considered as a probable source of positioning quality deterioration within CONUS coverage zone in the period before 20.05 UT.

2) There are two apparent periods of the CONUS area covered shrinking on February 15th, 2011. The first period lasts from 14.30 to 18.00 UT and generally coincides with the WAAS alerts (Fig.1 a). But according to the TEQC output data the real positioning quality is worse within the second period from 19.30 to 22.00 in comparison to the period from 14.30 to 18.00 UT. However WAAS does not provide any alerts for this second period of positioning quality decreasing;

3) WAAS alerts displays the lowest percent of the CONUS area covered which is less than 70% at 17.40 UT for LPV200 service (Fig.1 a). This value is much lower in comparison to the correspondent TEQC output results with is about 90% at the same time point (Fig. 8, right panel). We can consider such a mismatch as probable false alarm event in WAAS output.

4) There are certain events of the positioning quality deterioration at 09.00-09.30 UT, at about 15.00 UT and at about 20.00 UT for both Feb.14th and 15th, 2011. As these events take place on both days and at the same time points they probably have nothing to do with ionospheric disturbances. These events can be probably caused by such regular events as "local spots of bad visibility" of the

DOI: https://doi.org/10.30564/jasr.v2i1.343

GPS SV constellation. Such events can bring periodic regular variations of the local PDOP values which can repeat and move in local areas.

Generally there is a significant mismatch between TEQC output data and the WAAS alerts figure on both February 14 and 15 2011. It can be explained as we did not use any ranging corrections and we get the lower percent of the area covered in comparison to the WAAS alert figure. Some cases, however, can be considered as probable WAAS output mismatch information or false alarm but in order to prove it we need to crosscheck the data involving additional independent means of positioning availability control.

Fig.9 displays the percent of Canada area covered versus UT. We can see that the percent of area covered was not decreasing lower than 80% for all protection limits neither on June 20th (background day) no on June 22nd (initial and main phases of the geomagnetic storm).

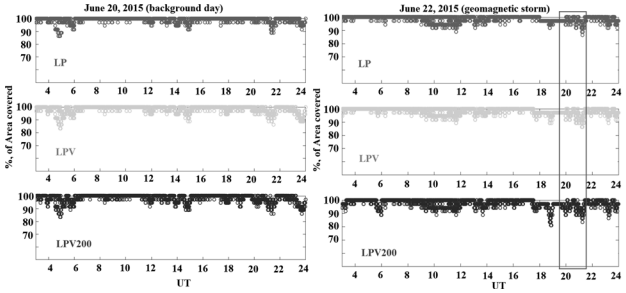

Figure 9. TEQC output: percent of the Canada area covered vs the UT on June 20th (left panel) and on June 22nd (right panel), 2015. The red rectangle marks the time period which corresponds to the WAAS alerts (see Fig 3b)

In contrast to the previous case the WAAS official alert gives significant percent of area covered shrinking which is expected from 19.45 to 21.35 UT on June 22, 2015 as a consequence of the strong geomagnetic storm (see Table 3). On the other hand there were not cases of the system outages on June 22nd, thereby the positioning deterioration events can be certainly considered as consequence of the ionospheric geomagnetic disturbances. According to Fig 9 we can find following results:

1) TEQC output data displays that positioning quality is generally worse on June 22nd, 2015 in comparison to the previous geomagnetically quiet day. It is especially true for the time period from 17.30 to 22.00 UT on June 22nd (Fig. 9, right panel). This time period partially coincides with the WAAS alert (Table 3) but TEQC output data gets 85% of the lowest % of area covered that is in 20% higher in comparison with the WAAS alert data (Fig.3b).

2) Like the previous case there are certain events of the positioning quality deterioration at 05.00 UT, at about 14.00 UT, at about 21.30 UT and at 23.30 UT for both June 20 and 22, 2015. As these events take place on both days and at the same time periods they can probably be explained with the regular variations of the local PDOP values like previously.

3) There is a period of significant shrinking of the % of area covered at about 05.00 to 05.30 UT on June 20, 2015 (Fig 9, left panel). It was a background geomagnetically quiet day so this event has nothing to do with the geomagnetic storm impact. However, we should note that the most part of Canada is within the auroral oval area even under the geomagnetic quiet days. Such environment can bring ionospheric disturbances and GNSS signal quality deterioration even under a geomagnetically quiet condition [7].

Generally both TEQC output data and the WAAS alerts figure display an obvious shrinking of the % of area covered in Canada area on June 22nd, 2015 in the time period from about 09.00 to 22.00 UT under geomagnetic storm condition. This time period mostly corresponds to the main phase of the storm. Regardless we did not use any ionospheric correction the lowest % of area covered for the TEQC output data is in 20% higher in comparison with the WAAS alert figure. It can be considered as probable mismatch information or false alarm at the WAAS output.

3.2 Model Protection Levels and WAAS Alerts Comparison

A comparison between the previous results and the results of "model" protection levels computation based on (2) and (3) was conducted. Fig.10 displays the percent of CONUS area covered versus UT as a result of HPL (VPL) model computation. As it was defined in the previous section the time resolution of HPL and VPL computation was 5 minute. This time period corresponds to the period of the GIVE values computation in a real WAAS [11].

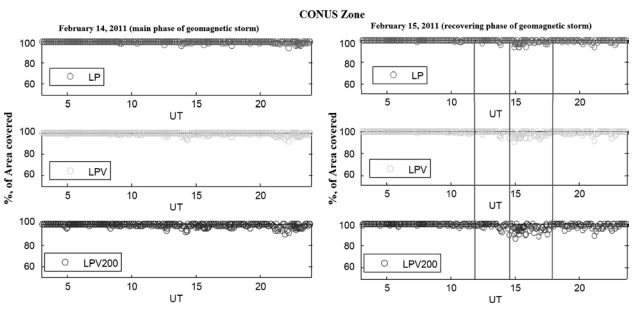

Figure 10. Modeling results: percent of CONUS area covered vs Time on Feb. 14th (left panel) and on Feb. 15th (right panel), 2011. Red lines mark approximate time points which correspond to WAAS alerts (see Fig 1 a).

Comparison between Fig.10 (left panel) and the WAAS alert figure on February 14th (Fig 1, b) displays general

 DOI: https://doi.org/10.30564/jasr.v2i1.343

accordance, especially for LPV200 service. According to the modeling results the lowest percent of area covered was about 93% for the LPV200 at 22.00-22.30 UT. It was expected that this value should be lower in comparison with the correspondent WAAS LPV200 alert figure on February 14th, 2011 (Fig.1 a), because we did not use any ionospheric correction in model computation (2).

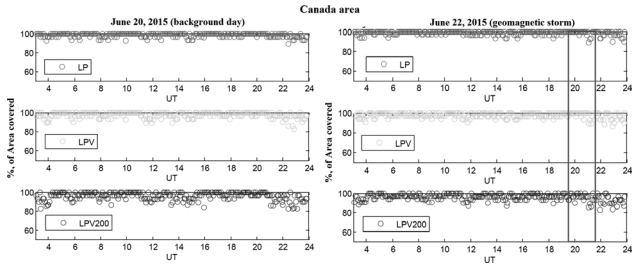

Figure 11. Modeling results: percent of Canada area covered vs Time on June 20th (left panel) and on June 22nd (right panel), 2015. The red rectangle marks the time period which corresponds to the WAAS alerts (see Fig 3 b).

The HPL (VPL) modeling computation displays lower % of the CONUS area covered on February 15th, 2011 in comparison to the previous day. The events of the lowest % of area covered takes place in the time period from 14.00 to 18.00 UT (Fig. 10, right panel) which is generally coincides with the WAAS alert figure (Fig.1 a). Nevertheless the lowest percent of the area covered was 85% at about 15.00 UT for the model computation which is in 8-10% less in comparison with the WAAS alert figure for the same time. On the other hand the LPV200 modelling computation gets about 95% of the area covered at 17.30 UT which is in 30% higher in comparison with the WAAS alert for the same time point (Fig.1 a). As the modelling results gets similar figure to the TEQC output data we can suppose that such mismatch of alert figures between the WAAS data and our modeling results displays probable WAAS false alarm in protection levels computation in this time period.

Fig.11 displays the percent of Canada area covered versus UT as a result of the HPL (VPL) model computation. In contrast to the previous case this modelling computation displays obvious accordance neither the WAAS alert figure (Fig.3) nor the real positioning quality figure (Fig.9). Generally we can see random character of the model LP (LPV) computation results but there are events of the % of the area covered decreasing at about 04.00 UT, 12.00 UT and 23.00 UT on both June 20th and June 22nd, 2015. Probably it can be explained with periodic regular variations of the local PDOP values in the same local areas.

There is no obvious decreasing in percent of the Canada area covered within the time period from 19.30 to 21.30 UT on June 22, 2015, so there is no accordance between the modelling results and the WAAS alert figure this time. There is no significant difference between the modeling computation results for June 20th and June 22nd, 2015 data in Fig 11. However the lowest value of the % of the Canada area covered was not lower than 80 % for all protection levels on both days of the observation. For the LPV 200 protection level this value is in 15-20% higher comparing to the WAAS alert figure (Fig.3 b). Therefor we see probable mismatch of alert figures between the WAAS data and our modeling results in above mentioned environment again.

4. Discussion and Conclusion

Firstly, we should point out the random character of the modelling computation results on June 20-22nd, 2015 again(Fig 11). One of the probable explanations can be that there was the lack of GPS- sites we used to compute pro-tection levels in Canada area. On the other hand there is a big difference between radio propagation media in iono-sphere above the CONUS and the Canada areas.

Fig 12a displays the position of the south border of the auroral oval versus the UT on June 20th (solid green line) and on June 22nd, 2015 (dashed red line). This figure was derived based on the geophysical data (https://iswa.gsfc.nasa.gov/IswaSystemWebApp/). According to the figure we can see that most of the Canada is within the auroral oval on both geomagnetically quiet and, especially, stormy days. It drives us to think that most of the GPS SV line-of-sight pass through high-latitude ionosphere which always contents multi-scale ionospheric irregularities in contrast to the mid-latitude ionosphere (i.e. above the CONUS zone). The main conclusion rises that we may not use the same solution and the same data set of WAAS reference stations (WRS) to reconstruct the ionospheric GIVE values in the same manner for both Canada and CONUS areas.

There is no obvious accordance in time behavior between the modeled LP (LPV) time series (Fig. 11, right panel), dynamics of the ovation prime energy flux of electrons and ions (Fig.12 b) and dynamics of the auroral oval south border(Fig 12a). On the other hand a coincidence in time can be noticed between the WAAS alert (Fig.2 b) and peak of the ovation prime energy flux of electrons and ions at 20.00 UT (Fig.12 b). It is interesting result which displays a contradiction between the real positioning quality and expected protection levels based on the model representa-tions of the GIVE values.

Regardless the peak of the ovation prime energy flux took place at 20.00 UT the most part of the flux energy fell on the North Atlantic, Europe and North of Russia that

DOI: https://doi.org/10.30564/jasr.v2i1.343

time. Indeed we can see that this energy flux did not bring significant motion in the south border of the auroral oval in the North America (Fig.12a). On the other hand the first lower peak of the ovation prime energy flux at 07.00 UT (Fig.12b) mostly fells on the North America and inspired significant shifting in the auroral oval border toward the south. However it did not bring noticeable features in both WAAS alert figure and real positioning quality results.

Our results display some cases of significant mismatch between the WAAS alert figure and real positioning quality for both the CONUS zone and Canada. This mismatch was proved by means of the model computation of HPL (VPL) values based on the real ionospheric ranging errors which were derived from the GPS sites within CONUS zone and Canada. The WAAS alerts got the expected percent of area covered which is much lower in comparison to the real positioning data for both the GPS standalone mode and the model HPL (VPL) computation in the most cases under consideration.

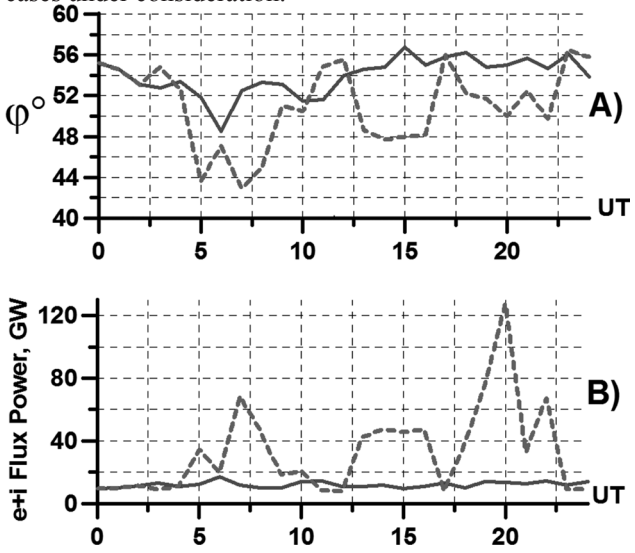

Figure 12. South border of the auroral oval dynamics and solar particles energy: panel a) position of the south border of the auroral oval vs time on June 20th (solid green line) and on June 22nd, 2015 (dashed red line); panel b) ovation prime energy flux (electrons+ ions precipitation within aurora) vs time on June 20th (solid green line) and on June 22nd, 2015 (dashed red line).

As it was shown the WAAS integrity service provides general response on the geomagnetic storm. Some particular cases, however, can be considered as probable false alarm of the HAL (VAL) exceeding. Indeed the WAAS alert figure gives much lower expected positioning availability under the geomagnetic storm conditions in comparison to our results at 17.40 UT on February 15th, 2011 and at 19.45-21.35 UT on June 22nd, 2015. In the first case, the real positioning quality according to the LPV and LPV200 requirements is provided more than 90 % percent of the CONUS area covered. This value is much higher comparing to the correspondent WAAS report (less than 70%) for the same conditions. Model HPL and VPL computation based on the real ionospheric ranging errors get the lowest percent of the area covered which is about 93% for CONUS zone. And again this is much higher in comparison to the WAAS alert figure for the same date and time.

We should emphasize that much better agreement between WAAS alert figure, real positioning and modelling data was achieved for the event on February 15th, 2011 in comparison to the one on June 22nd, 2015. It probably proves that the WAAS algorithm reacts better on the system outages events (see Table 2) than on geomagnetic storm, especially under high-latitude ionosphere environment. In our opinion such disagreement between the WAAS alert figure and our computation results can be caused by multi-scale ionospheric irregularities which are generated in the period of geomagnetic storm and can disrupt the correct GIVE values computations.

Based on the long time previous results it has been accepted that geomagnetic storms bring increasing in intensity of all-scale disturbances of the ionospheric total electron content (TEC) within the Globe [17,18,19]. This idea was reflected in the GPS and WAAS ionospheric standard models which are in the base of GIVE value computations. Such approach however is not able to take into account the real multi-scale ionospheric disturbances. These disturbances mostly affect GNSS performance in local areas which are associated with the travelling pattern of the ionospheric irregular structure not only in high and low latitudes bot also in mid-latitudes.

In spite of the mid-latitude ionosphere usually does not contain the sources to generate significant multi-scale ionospheric disturbances both the equatorial and the polar areas can bring ones into the mid- latitudes especially under magnetic storm conditions [20-22]. Low-latitude ionosphere contents specific ionospheric disturbances which are known as “ionospheric super-bubble”. These “bubbles” can penetrate in mid-latitudes up to 35-37°N under geomagnetic storm conditions [21]. On the other hand polar ionosphere can be a source of strong large-scale travelling ionospheric disturbances which are generated within the pulsing boarder of the auroral oval area and propagate toward the mid-latitudes as well [7].

Analyzing the ionospheric effects of numerous of magnetic storms in a period from 2000 to 2004 it was found that a region with intense with multi-scale electron density irregularities emerges during magnetic storms on the border of the auroral oval. The region of increased in-

 DOI: https://doi.org/10.30564/jasr.v2i1.343

tensity of these irregularities can have a large spatial scale (hundreds and thousands kilometers) and travel following the uniformly moving or pulsating auroral oval border [7]. The instantaneous pattern of ionospheric irregularities distribution is heterogeneous in space and rapidly changes in time. It means that we must not expect global concurrent effect of the geomagnetic disturbances in GNSS and WAAS performance. It is more likely that the geomagnetic storm effects bring local sharp positioning quality deterioration. It can happen suddenly anytime not only within the main phase of geomagnetic storm but also within during its recovering phase.

All the above mentioned probably tells that it is necessary to revise the main WAAS building concept taking into account the latitudinal features of the ionosphere. The main concept of the WAAS integrity monitoring is that the confidence bounds of expected ranging errors must be large enough to describe the error in the correction, but tight enough to allow the operation to proceed. If it is not possible to distinguish between nominal and disturbed conditions, then we must always assume disturbed conditions are present. As we could see earlier this concept may get false alarm.

In case the main concept of the WAAS integrity monitoring has to stay the same, there are two main ideas to solve the above mentioned contradiction. Firstly, we can find a solution to detect ionospheric irregularities so that we can provide a high level of service during undisturbed time periods [23,24]. A reduced level of expected service would only be necessary during periods of detected ionospheric disturbances [23]. In order to realize this solution in practice the detection scheme of the ionospheric disturbances must be extremely robust, in order to provide the necessary level of protection. The integrity requirements for precision approach guidance set the probability of hazardously misleading information below 10^{-7} per approach. Therefore, the chance of an undetected ionospheric irregularity must be at a similarly small level. Taking into account the above mentioned, it is unlikely to achieve such high probability of undetected multi-scale ionospheric disturbances even in mid-latitudes let alone high and low latitude areas.

Secondly, WAAS can also be modernized to take advantage of new signals of all global positioning systems (GLONASS, BeiDou, GALILEO, QZSS etc) and GEOs. Indeed by only upgrading the WAAS Reference Station (WRS) receivers to measure Galileo signals we can double our sampling of the ionosphere. The increased sampling translates into smaller broadcast confidence values on the single frequency ionospheric corrections. These lower values lead to higher availability. Similarly, the L5 signal has better noise properties and can be acquired at a lower elevation angle. This leads less uncertainty in the ionospheric measurements and to smaller confidence bounds as well [25]. In reality, however, serious unpredicted obstacles were unfolded in common multi-system signal data processing. GPS TEC measurements for the GIVE computation, although highly precise, are often rendered inaccurately due to satellite and receiver differential code biases (DCBs). Calculated satellite DCB values are now available from a variety of sources, but receiver DCBs generally remain an undertaking of the receiver operators and processing centers [26,27,28].

The other serious problem here is comprised in significant difference in ranging errors accuracy from all current positioning system and another ranging data sources. For example, a consistent analysis of signal-in-space ranging errors (SISREs) was conducted for all current satellite navigation systems, considering both global average values and worst-user-location statistics. Global average SISRE values for the individual constellations amount to 0.7 ± 0.02 m (GPS), 1.5 ± 0.1 m (BeiDou), 1.6 ± 0.3 m (Galileo), 1.9 ± 0.1 m (GLONASS), and 0.6 ± 0.2 m (QZSS) over a 12-month period in 2013/2014 [27].

Besides this we should take into account that some anomalies in particular SV ranging are also possible. As an example of it GPS satellite oscillator anomalies mimicking ionospheric phase scintillation can be pointed out. Such ranging anomalies can be expected from an anomaly in the satellite's oscillators which are a persistent phenomenon. They have the potential to generate false alarms in the systems to forewarn of GPS outages due to the ionospheric scintillation [29,30].

And finally, the capability of GNSS receivers to track multiple GNSS signals poses the problem of mutual alignments of reference frames and time scales [31]. System biases should possibly be computed in advance and made known to the user, so that the only unknowns for code point positioning are the receiver coordinates and the receiver clock offset relative to a unique time scale [28].

In our opinion in order to achieve high confidence of WAAS positioning availability alerts real ionospheric measurements within the wide area coverage zone must be involved instead of the WAAS GIVE values [33]. The better way to realize this idea is to combine the WAAS and LAAS solutions. According to [12] in order to form the ranging confidence bounds the real ranging which were collected from WRSs in WAAS coverage zone are decomposed as following

$$\sigma_{TOT}^2 = \sigma_{flt}^2 + \sigma_{UIRE}^2 + \sigma_{air}^2 + \sigma_{trop}^2 \quad (7)$$

DOI: https://doi.org/10.30564/jasr.v2i1.343

These terms correspond to: the satellite clock and ephemeris corrections error (σ_{flt}), the ionospheric correction error (σ_{UIRE}), the code noise, multipath error (σ_{air}), and the troposphere error (σ_{trop}).

According to their impact on the final UDRE and GIVE values we can divide these errors into two groups: 1) the global ranging correction errors which do not depend on the user's location within WAAS coverage zone and 2) the locally dependent ranging correction errors which are strictly dependent on the user's position within WAAS coverage zone. The first group of the errors contains the satellite clock and ephemeris corrections error (σ_{flt}) as well as differential code biases for SVs and the second group shell include tropospheric, ionospheric and multipath errors.

WAAS can provide high confident corrections and integrity monitoring for the first group ranging errors within the coverage zone in any geophysical environment. On the other hand the σ_{UIRE}, σ_{air} and σ_{trop} components are strictly dependent on the local environment of radio wave propagation. There are a numerous research which proves low confidence of locally dependent ranging corrections under geomagnetic storms, solar radio flares and another irregular external impacts. Probably it means that better solution is to get these ranging error statistics not from WAAS output but from the local GNSS-sites output. Today there are several types of such local GNSS networks which can be considered to involve in the above mentioned implementation: Geodynamics and geophysical services network, like GEONET, IGS, RTK-networks; Local Area DGPS; the WAAS WRSs sites etc.

The σ_{UIRE}, σ_{air} and σ_{trop} statistics can be collected at the above mentioned local GNSS sites and broadcast to the nearest users within a local coverage zone. Combining "global" ranging correction with locally dependent ranging corrections the user equipment can use both WAAS and Local network ranging data statistics to compute correspondent HPL (VPL) with higher confidence.

Acknowledgments: This work is supported by the Chinese Academy of Sciences (CAS) program of "Light of West China" (Grant No. 29Y607YR000103), Chinese Academy of Sciences, Russia and Ukraine and other countries of special funds for scientific and technological cooperation (Grant No. 2BY711HZ000101) and the Russian Science Foundation Grant No. 17-77-20005. The second author is financially supported by the China Scholarship Council (CSC) for his visiting postdoctoral research at the German Research Centre for Geosciences (GFZ).

References

[1] Global positioning system wide area augmentation system (WAAS) performance standard (2008). Appendix B, 1st Edition

[2] Tossaint M, Samson J, Toran F, Ventura-Traveset J, Hernandez-Pajares M, Juan JM, Sanz J, Ramos-Bosch P (2007), "The Stanford—ESA integrity diagram: a new tool for the user domain SBAS integrity assessment", *Navigation*, Institute of Navigation, 2(54), 153–162. https://doi:10.1002/j.2161-4296.2007.tb00401.x

[3] Datta-Barua S, Lee J, Pullen S, Luo M, Ene A, Qiu D, Zhang G, Enge P (2010), "Ionospheric threat parameterization for local area Global-Positioning-System-based aircraft landing systems", J Aircraft, 47(4), 1141–1151. https://doi:10.2514/1.46719

[4] Kintner PM, Kil H, and E. de Paula (2001), "Fading Time Scales Associated with GPS Signals and Potential Consequences", *Radio Science*, 36(4), 731–743. https://doi:10.1029/1999RS002310

[5] Paulo L, Fortes S, Lin T, and Lachapelle G (2015), "Effects of the 2012–2013 solar maximum on GNSS signals in Brazil", *GPS Solutions*, 19, 309–319. doi:10.1007/s10291-014-0389-1

[6] Sieradzki R and Paziewski J (2016), "Study on reliable GNSS positioning with intense TEC fluctuations at high latitudes", *GPS Solutions*, 20, 553–563. https://doi:10.1007/s10291-015-0466-0

[7] Afraimovich EL, Astafyeva EI, Demyanov VV, and Gamayunov IF (2009), "Mid-latitude amplitude scintillation of GPS signals and GPS performance slips", *Advances in Space Research*, 43, 964–972. https://doi.org/10.1016/j.asr.2008.09.015

[8] Wide-area augmentation system performance analysis report, Report #36. Reporting Period: January 1 to March 31, 2011. Available from: http://www.nstb.tc.faa.gov/DisplayArchive.htm

[9] Wide-area augmentation system performance analysis report, Report #53. Reporting Period: April 1 to June 30, 2015. Available from: http://www.nstb.tc.faa.gov/DisplayArchive.htm

[10] Estey L. and Meertens C (1999), "TEQC: The Multi-Purpose Toolkit for GPS/GLONASS Data", *GPS Solutions*, 3(1), 42-49. https://doi:doi:10.1007/PL00012778

[11] SARPS Amendment 77, Annex 10 to the Convention on International Civil Aviation, Aeronautical Telecommunications: International Standards and Recommended Practices, Volume 1, Radio Navigation Aids, November 2002

[12] Mimimum Operation Performance Standard: MOPS

 DOI: https://doi.org/10.30564/jasr.v2i1.343

DO-229C. Version C, Appendix A: Wade Area Augmentation System Signal Specification, 2001 RTCA Inc.

[13] Mylnikova AA, Yasyukevich YV, Kunitsyn VE, and Padokhin AM (2015), "Variability of GPS/GLONASS differential code biases", *Results in Physics*, 5, 9–10. https://doi.org/10.1016/j.rinp.2014.11.002

[14] Schaer S (2012), "Overview of GNSS biases. International GNSS Service. Workshop on GNSS Biases". [Electronic resource]. URL: http://www.biasws2012.unibe.ch/pdf/bws12_1.3.1.pdf

[15] Hilla S, and Cline M (2004), "Evaluating pseudorange multipath effects at stations in the National CORS Network", *GPS Solutions*, 7, 253–267. https://doi.org/10.1007/s10291-003-0073-3

[16] Xia L (2004), "Multipath in GPS navigation and positioning", *GPS Solutions*, 8, 49–50. https://doi.org/10.1007/s10291-004-0085-7

[17] Lekshmi DV, Balan N, Ram ST, and Liu JY (2011), "Statistics of geomagnetic storms and ionospheric storms at low and mid latitudes in two solar cycles", *Journal of Geophysical Research*, 116, A11328. https://doi:10.1029/2011JA017042

[18] Jakowski N, Mayer C, Wilken V, Borries C, and Doherty PH (2007), "Ionosphere Storms at High and Mid-latitudes Monitored by Ground and Space Based GPS Techniques", *Proceedings of the International Beacon Satellite Symposium*, Boston College, June 11–15, Boston, USA

[19] Aarons J, Mullen JP, Whitney H. [et al.] (1981), "VHF Scintillation Activity Over Polar Latitudes", *Geophysical. Res. Lett*., 8, 277–280. https://doi:10.1029/GL008i003p00277

[20] Afraimovich EL, Astafieva EI, Demyanov VV (2004), "Ionosphere Geomagnetic Variations and GPS Positioning Errors During the Major Magnetic Storm on 29–31 October 2003", *International Reference Ionosphere News*, 11 (3–4), 10–14

[21] Demyanov VV, Yasyukevich YV, Ishin AB, and Astafyeva EI (2012), "Effects of ionosphere super-bubble on the GPS positioning performance depending on the orientation relative to geomagnetic field", *GPS Solutions*, 16, 181-189. https://doi.org/10.1007/s10291-011-0217-9

[22] Veettil SV, Haralambous H, and Aquino M (2017), "Observations of quiet-time moderate mid latitude L-band scintillation in association with plasma bubbles", *GPS Solutions*, 21, 1113–1124. https://doi.org/10.1007/s10291-016-0598-x

[23] Walter T, Blanch J, and Rife J (2004), "Treatment of Biased Error Distributions in SBAS", Presented at the International Symposium on GNSS/GPS, December, 2004, Sydney, Australia [Electronic resource]. – Stanford, 2004. URL: http://web.stanford.edu/group/scpnt/gpslab/pubs/papers/Walter_ISGNSS_2004.pdf

[24] Rife J, Walter T, and Blanch J (2004), "An Overbounding SBAS and GBAS Error Distributions with Excess-Mass Functions", Presented at the International Symposium on GNSS/GPS, December, 2004, Sydney, Australia [Electronic resource]. – Stanford, 2004. URL: http://web.stanford.edu/group/scpnt/gpslab/pubs/papers/Rife_IGNSS_2004.pdf.

[25] Walter T, Enge P, Reddan P (2004), "Modernizing WAAS", Presented at the International Symposium on GNSS/GPS, December, 2004, Sydney, Australia [Electronic resource]. – Stanford, 2004. URL: http://web.stanford.edu/group/scpnt/gpslab/pubs/papers/Walter_IONGNSS_2004.pdf.

[26] El-Mowafy A (2014a), "GNSS Multi-Frequency Receiver Single-Satellite Measurement Validation Method", *GPS Solutions*, 18(4), 553-561. https://doi.org/10.1007/s10291-013-0352-6

[27] Montenbruck O, Steigenberger P and Hauschild A (2015), "Broadcast versus precise ephemerides: a multi-GNSS perspective", *GPS Solutions*, 19, 321–333. https://doi.org/10.1007/s10291-014-0390-8

[28] Hakansson M, Jensen ABO, Horemuz M, and Hedling G (2017), "Review of code and phase biases in multi-GNSS positioning", *GPS Solutions*, 21, 849–860. https://doi.org/10.1007/s10291-016-0572-7

[30] Benton CJ, and Mitchell CN (2012), "GPS satellite oscillator faults mimicking ionospheric phase scintillation", *GPS Solutions*, 16, 477-482. https://doi.org/10.1007/s10291-011-0247-3

[31] Benton CJ, and Mitchell CN (2014), "Further observations of GPS satellite oscillator anomalies mimicking ionospheric phase scintillation", *GPS Solutions*, 18, 387-391. https://doi.org/10.1007/s10291-013-0338-4

[32] El-Mowafy A (2014b), "GNSS multi-frequency receiver single-satellite measurement validation method", *GPS Solutions*, 18, 553-564 https://doi.org/10.1007/s10291-013-0352-6

[33] Demyanov VV, and Likhota RV (2015), "The method of GNSS positioning availability control for transportation applications", *Machines, Technologies, Materials*, 5, 11-13. ISSN 1313-0226

DOI: https://doi.org/10.30564/jasr.v2i1.343

BILINGUAL PUBLISHING CO.
Pioneer of Global Academics Since 1984

Journal of Atmospheric Science Research
http://ojs.bilpublishing.com/index.php/jasr

ARTICLE

Cogeneration Potential in the Industrial Sector and Gas Emission Reduction: A Case Study

Natália de Assis Brasil Weber Hirdan Katarina de Medeiros Costa*

Institute of Energy and Environment, Universidade de São Paulo, São Paulo, 1289, São Paulo-SP, Brazil

ARTICLE INFO

Article history
Received: 2 December 2018
Accepted: 2 January 2019
Published: 7 March 2019

Keywords:
Air pollution
Fuel replacement
Cogeneration system
Decentralized generation
Industrial sector

ABSTRACT

The aim of the current paper is to discuss the replacement of diesel oil (DO) consumption by natural gas (NG) in a cogeneration system. A specific industrial consumption case study was chosen to be the method used to accomplish a robust analysis. The results have shown the advantages in reducing CO_2, CH_4, N_2O and particulate matter emissions, as well as the need to keep the NOx emission rates. After proceeding with theoretical studies concerning our case, we concluded that the diesel oil replacement by natural gas is beneficial for gas emission reduction. Public policies should consider local development based on the use of different fuels, such natural gas, to achieve the integration between decentralized energy generation and energy-efficient initiatives.

1. Introduction

The use of different fuels has become an important concern when it comes to Climate Change debate, to pollution impacts from local to global levels, as well as to lifestyle changes within modern society. Therefore, the use of low carbon alternative fuels began to gain more space in politics and public planning. Thus, many researches have been focused on diesel replacement to lesser pollutant fossil fuels, such natural gas [1, 2].

Society is now living a time when its demands regarding amenities provided by different forms of fuels are clear. Thus, it is mandatory to think, create and build practices that meet community demands in order to help solving the emerging environmental problems.

The aim of the current paper is to discuss local development based on replacement of fuels (natural gas instead of diesel) in order to achieve the integration between decentralized energy generation and energy-efficient initiatives. Our study is based on a specific industrial consumption case study to accomplish a robust analysis, specifically the cogeneration potential in the industrial sector of Novo Hamburgo City.

Thus, in order to achieve our goal, section 2 exposes the literature review. Section 3 includes our methods. Section 4 shows our results. Finally, section 6 presents our conclusions.

2. Literature Review

2.1 Combined Heat and Power (CHP)

CHP or cogeneration consists of a way to produce heat

**Corresponding Author:*
Hirdan Katarina de Medeiros Costa,
Institute of Energy and Environment, Universidade de São Paulo, São Paulo, 1289, São Paulo-SP, Brazil
E-mail: hirdan@usp.br

DOI: https://doi.org/10.30564/jasr.v2i1.419

and power within the same system. Such technology provides two ways of using energy from the same fuel, minimizing wastes. There is a vast literature on CHP. It demands lower costs and causes lesser GHG emissions than other electricity and heat production mechanisms [3].

Conventional electricity generation systems are usually centralized, and in Brazil it is mainly based on thermal and hydroelectric powerplants. Within such concept, it is necessary to invest in long electricity transmission and distribution lines in order to connect the centralized generation to the customers, in other words, to a distributed demand [4].

On the other hand, it is possible to produce energy in a decentralized pattern way. This method is called distributed generation and its main feature is that electricity generation is close to the consumer point [5, 6, 7].

The benefits of adopting CHP as a distributed generation source are: elimination of technical losses in transmission and distribution [8]; diversification of the energy matrix [9, 10]; decreased energy intensity [9]; improved energy efficiency [11]; fulfillment of GHG reduction targets [12]; and CO_2 emission reduction [11].

Ouellette et al. [12] found that the implementation of a CHP system in Alberta may result in the approximately 15–24% CO_2 reduction expected by the 2008 Alberta Climate Strategy. Thus, CHP implementation could bring up significant contributions to the achievement of the Kyoto Protocol's emission reduction targets [11].

Cogeneration also presents negative points such as the need to invest in CHP equipment, a more complex and demanding operation and the lack of technical training, as it was already stressed by Andreos [5] and Baer et al. [13]. Also, Baer et al. [13] have pointed out that CHP installations have high upfront costs and long payback periods, when they are compared to traditional equipment.

CHP has been mainly used by industries and for district heating worldwide [14, 15, 16]. It has been analyzed as part of a system involving the eco-industrial park concept (EIP) [17]. According to some authors, local heating systems distribute the centralized-generated heat in a residential and sometimes commercial location, managed at low costs [18, 19].

Chung et al. [20] analyzed a CHP plant case study applied to a set of buildings such as residential buildings, offices, hospitals, stores, and schools in Korea. They found that the payback period might be of approximately two years in buildings investing in a generator with the capacity to hold 50% of their electricity peak demand.

Nowadays, several countries are developing their own policies to promote small-scale cogeneration in the residential sector. Small-scale residential cogeneration systems are widely recognized as efficient systems and they have an important potential for energy and economic saving [21, 22]. They are often used in industries that use their on waste as a fuel such as the sugarcane, chemical, petrochemical and pulp and paper industries.

Brazil had only 550 working cogeneration units up to 2000. However, this scenario began to change in 2010 when this indicator went up to 851 units. Today, the country has approximately 943 working cogeneration units [23]. In addition to such fact, the recent discovery of the pre-salt layer in the Santos basin doubled the Brazilian oil and gas reserves, leading the country's gas market to a favorable scenario [5].

The installed cogeneration capacity in Brazil will reach its peak (14,056.0 MW) in 2015, time when it is going to have the same production as Itaipu hydroelectric powerplant, which has an installed capacity of 14,000 MW [5].

Hwang [24] pointed out many studies that evaluate the efficiency of this process in industries. Hwang [24] looked for ways to improve existing technologies or even for possible innovative cogeneration uses in different industrial processes.

The present research aims to determine the cogeneration potential in the industrial sector of Novo Hamburgo City, by considering the importance of implementing integrated decentralized energy generation and energy-efficient initiatives. The analysis was made through the replacement of diesel oil (DO) consumption by natural gas (NG) in a CHP system in the industrial sector of the abovementioned city.

Natural gas has been pointed out as a transition fuel that will facilitate the insertion of renewable fuels [4, 1, 2]. There is a lot of research studying the use of renewables such as biogas in the cogeneration process [25, 26]. Additionally, Celma et al. [27] and Andersen and Lund [28] have pointed out that CHP systems, along with the renewable energies (solar, wind, biomass etc.), are key elements for future cleaner energy policies.

Usually, the heat and power production in a cogeneration system releases considerable amounts of GHG into the atmosphere. Accordingly, the study by Aldrich et al. [29], is an attempt to expose and evaluate different allocation methods, to apply them to a combined heat and power plant integrated to a paper mill, and to propose an alternative method to better calculate the efficiency of the process.

Finally, the present research is an attempt to show that there are alternative fuels ready to be consumed in the study area, such natural gas (a fossil fuel lesser pollutant than diesel). However, investors lack information on the feasibility of the project [30]. Therefore, we also show the

 DOI: https://doi.org/10.30564/jasr.v2i1.419

possibility of reducing local environmental impacts, and the feasibility of using already established technology in the electricity production market at lower costs.

It is worth minimizing the emission of pollutants resulting from the decentralized CHP conversion process, since it is often located close to urban perimeters. Thus, it is important to present the results by Fahlén and Ahlgren [31], who account for the social and environmental costs of the local heating process when the option for using CHP technologies is made. Fahlén and Ahlgren [31] pointed out that the use of district heating processes is just justified when natural gas is used as fuel.

3. Material and Methods

The methods used in the current study consist of a case study, considering quantitative and qualitative approaches.

The case study concerns a Decentralized Energy Plan (DEP) in Novo Hamburgo City, which is located in the metropolitan region of Porto Alegre, Rio Grande do Sul State, Brazil. This case study focuses on the Novo Hamburgo industrial sector and is divided in 4 parts:

a. Industrial sector evaluation;

b. Fuel replacement evaluation, from DO to NG;

c. CO_2 emissions reduction evaluation.

The DEP of Novo Hamburgo is part of a data acquisition system initiated in 2011 during the research project: "The data survey, the analysis of energy diagnosis, and the evaluation of potential renewable sources in Novo Hamburgo County" [32]. The study was conducted in State University of Rio Grande do Sul under the supervision of Professor Elton Gimenez Rossini.

However, in 2015, the study faced changes and updates in order to evaluate the replacement of DO by NG in a CHP system.

Thus, the present research aim to contribute to integrate an environmental analysis towards an eco-industrial park (EIP) program in Novo Hamburgo's industrial park when it comes to the industrial ecology (IE) field. As Korhonen [33] (p. 509) have stated, the IE concept draws "from the metaphor that a natural ecosystem is a vision for industrial environmental management and environment policy."

3.1 Assumptions

The following assumptions were made in order to compare the use of DO and its replacement by NG in a cogeneration system at the municipal industrial sector:

A. The DO generator specific fuel consumption considered was 0.26 l/kWh. Based on an efficiency of the generator of 38%, a typical calorific value of 10,500 Kcal/kg, and a capacity factor rated 70% of nominal capacity;

B. The NG generator specific fuel consumption considered was 0.3m³/kWh. Based on an efficiency of the generator of 35%, a typical calorific value of 8,560 Kcal/m³, and a capacity factor rated 80% of nominal capacity;

C. The cogeneration system considered the same temperature in all systems presenting 85% efficiency, and 80% of capacity factor; so, the total system efficiency is 68%;

D. An ICE (Internal Combustion Energy) fueled by NG and with power capacity of 100kW per consumer, operated for 12 hours a day, 22 days a month, which is equivalent to 3168 hours a year;

E. Only the following industries were considered likely to substitute DO generation by NG in a cogeneration system: the metallurgical, mechanical, chemical, textile, food and beverage industries.

3.2 Calculation

3.2.1 NG Evaluation for DO Replacement

Equations 1, 2 and 3 summarize the calculations to evaluate the amount of necessary NG in a CHP system to replace the DO consumed in the industrial sector in one year.

$$EEj = \sum_{j=1}^{n} DOtj \times SFCdo \tag{1}$$

$$NGj = \sum_{j=1}^{n} \frac{EEj}{SFCng} \tag{2}$$

$$NGcoj = \sum_{(j=1)}^{n} NGj \times Efng \tag{3}$$

Where: DOt = total diesel oil consumption by the industrial sector, in liters, l; SFCdo = specific fuel consumption of diesel generator, l/kWh; NG = natural gas consumption to generate the same amount of energy generated by diesel oil, m³; EE = electric energy generated by diesel oil, kWh; SFCng = specific fuel consumption of natural gas generator, m³/kWh; NGco = natural gas necessary to substitute diesel oil in a cogeneration process, m³; Efng = efficiency of natural gas generator; j = time considered, one year, 2013.

3.2.2 CO_2 Emission Estimation

We estimated the CO_2 emissions of the DO electric generation using a top-down approach designated by IPCC [34] against the emissions of the cogeneration system fueled by NG. Six (6) steps were used to evaluate CO_2 emissions the flowchart shows in summary all the steps.

DOI: https://doi.org/10.30564/jasr.v2i1.419

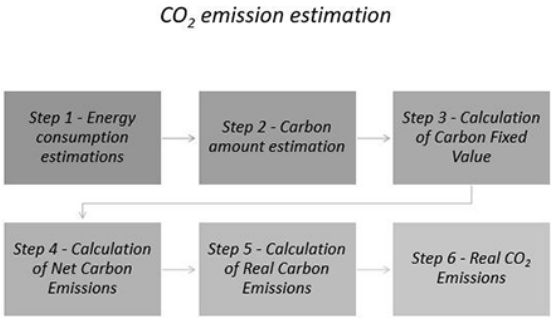

Figure 1. CO_2 emission estimation flowchart

Step 1: energy consumption estimations

It is necessary to multiply the fuel consumption by the following factors, namely: conversion factor (toe/fuel unit), correction factor[1] (dimensionless) from Higher Heating Value (HHV) to Lower Heating Value (LHV), and $45.2x10^{-3}$ TJ (equivalent to one Brazilian toe, in order to convert the energetic content from toe to TJ) in order to find the energy consumption in joules, as shown in Eq. (4). The parameters are shown in Table 1.

Table 1. Conversion factors for medium toe (toe/fuel unity)

	Diesel Oil	Natural Gas (cogeneration)
ConvF	0,848	0,857

Source: ELETROBRAS [35]; Ribeiro [36].

$$EC = FC \times ConvF \times CorrF \times 45.2 \times 10^{-3} \quad (4)$$

Where: EC = Energy Consumption (TJ); FC = Fuel Consumption (fuel unit); ConvF = Conversion Factor (toe/fuel unit); CorrF = Correction Factor[2] (dimensionless) of Higher Heating Value (HHV) to Lower Heating Value (LHV); $45.2x10^{-3}$ TJ = 1 Brazilian toe (to convert the energetic content from toe to TJ).

Step 2: Carbon amount estimation (GgC[3])

It applies the following equation, Eq. (5):

$$CA = EC \times EmissF \times 10^{-3} \quad (5)$$

Where: CA = Carbon Amount (GgC); EC = Energy Consumption (TJ); EmissF = Emission Factor (tC/TJ).

Considering data in Table 2.

Table 2. Carbon emission factors (GgC/TJ)

	Diesel Oil	Natural Gas
EmissF	20,2	15,3

Source: Ribeiro [36].

Step 3: Calculation of Carbon Fixed Value (GgC)

In this case, the carbon fixed value (CFV) equals zero, because there is no carbon energy consumption, since all the fuel is burned to generate electricity [35]. Thus, Eq. (6) equals zero.

$$FCA = 0 \quad (6)$$

Step 4: Calculation of Net Carbon Emissions (GgC)

Since the CFV is equal to zero, net carbon emissions (NCE) is equal to CA, as exemplified in Eq. (7).

$$NCE = CA - FCA \quad (7)$$

Step 5: Calculation of Real Carbon Emissions (GgC)

The RCE (GgC), Eq. (8), is the multiplication of the NCE (GgC) found in Eq. (7) by the OCF (dimensionless). The factors used for each type of fuel are shown in Table 3.

Table 3. Carbon Oxidized Fraction (dimensionless)

	Diesel Oil	Natural Gas
OFC	0,99	0,995

Source: Ribeiro [36].

$$RCE = NCE \times OCF \quad (8)$$

Where: RCE = Real Carbon Emissions (Gg C); NCE = Net Carbon Emissions; OCF = Oxidized carbon fraction (dimensionless).

Step 6: Real CO_2 ($GgCO_2$)Emissions

The real CO_2 emissions are obtained by Eq. (9).

$$RECO2 = RCE \times {}^{44}/_{12} \quad (9)$$

Where: $RECO_2$ = Real Carbon Dioxide Emissions (Gg CO_2); RCE = Real Carbon Emissions (Gg C); ${}^{44}/_{12}$ = Ratio between CO_2 and C molecular weights.

1 The used correction factor (Fcorr) to turn HHV into LHV are 0.95, for solid and liquid fuels, and 0.90, for the gaseous fuels [35, 36].

2 The correction factor (Fcorr) to transform the HHV in LHV, used are 0.95 for solid and liquid fuels and 0.90 for the gaseous fuels [35, 36].

3 GgC is a unit used to measure the mass of emitted CO_2 and it means Giga grams of CO_2, it is also common to be used tons of CO_2, or tCO_2.

 DOI: https://doi.org/10.30564/jasr.v2i1.419

4. Results and Discussions

Results are presented as follows.

4.1 Industrial sector evaluation

According to the Commerce, Industry and Services Association of Novo Hamburgo, Campo Bom and Estância Velha [37] the main industrial activities in Novo Hamburgo are: footwear, metallurgical, textile, and chemical industries. The city also stands out as a hub of trade and services [38]. Fig. 2 shows the number of industrial business registered at ACI-NH/CB/EV [37], in 2014, a total of 3,202 industrial companies are registered. The footwear sector accounts for 30% of this total, and it is followed by the metal sector, which represents 17% of the companies in this sector. It is worth noticing that only 1,293 of these companies have their industrial activities located in Novo Hamburgo County.

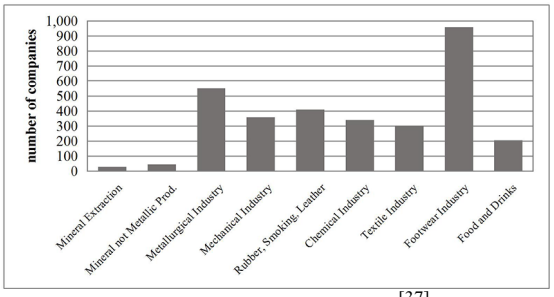

Source: ACI-NH/CB/EV, 2015 adapted by authors [37]

Figure 2. Industrial business types in Novo Hamburgo

The industrial sector aggregates energy consumption data from all industrial plants, in this case: 1,293 industrial plants. Energy consumption in this sector was characterized in 2013, and shown in Fig. 3. It is important to notice, that this sector is the only one presenting energy consumption reduction of approximately 12% between 2005 and 2013, probably because of the reduction in exports of footwear industry [32].

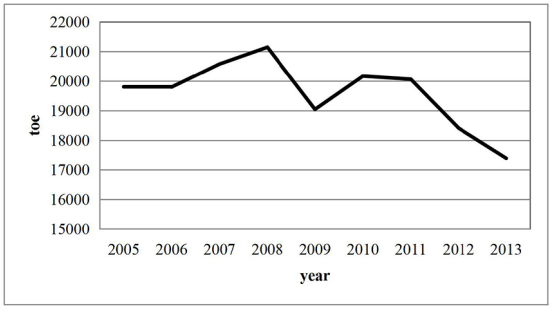

Figure 3. Total energy consumption in Novo Hamburgo's industrial sector (2005 – 2013)

Next, Fig. 4 shows the percentage of energy sources consumed by Novo Hamburgo's industrial sector; Diesel oil is the most consumed energy, thus accounting for 55% of all the energy consumed by the sector in 2013.

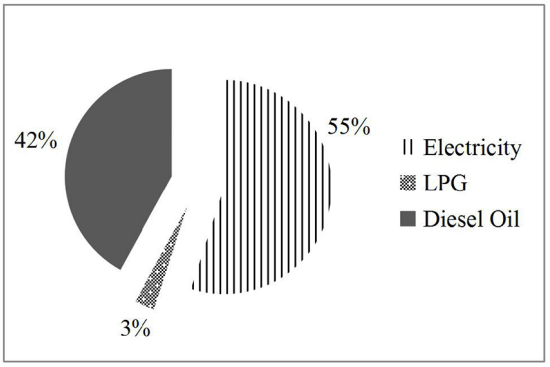

Figure 4. Energy consumption by source in the industrial sector of Novo Hamburgo in 2013

Energy consumption behavior can be analyzed through the final energy consumption related to the number of consumers within the main economic sectors. The final electricity consumption per consumer in Novo Hamburgo's industrial sector was similar to that of Rio Grande do Sul State up to 2010, approximately 147.6 MWh/end user, as shown in Fig. 5. In 2013, the electricity consumption per end user in Novo Hamburgo was 149.3 MWh/end user, growing at low rates.

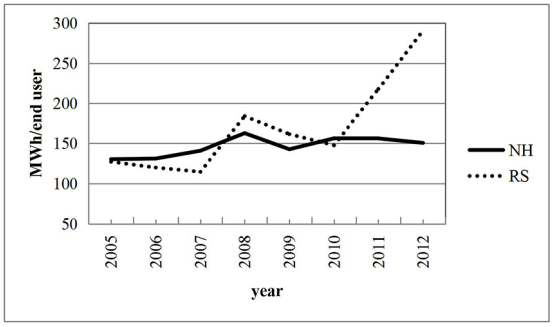

Source: Capeletto; Moura, 2014; Weber, 2014 adapted by authors, 2016[39]

Figure 5. Final electricity consumption according to the number of consumers in the industrial sector of Novo Hamburgo County and in Rio Grande do Sul State from 2005 to 2012 - MWh/end user

4.2 Fuel replacement evaluation, from DO to NG

According to Sulgás [40], companies subject to cogeneration use, in other words, those simultaneously demand electricity production and heat, i.e: engineering, food, beverage, chemical, automotive, textile, paper, non-ferrous and white ceramic industries, among others.

Therefore, considering such industries at Novo Hamburgo and also their energy consumption it was possible estimate the cogeneration potential. The estimated total

DOI: https://doi.org/10.30564/jasr.v2i1.419

number of industries able to use cogeneration systems in industrial production system was 213. The estimated mean consumption, according to the proposed methods, was 149.3 MWh/year, and 19,450 liters of DO per year. Values of NG use in a CHP system to replace DO are shown in Table 4, and they were based on the aforementioned data and on the assumptions originated from the herein proposed methods.

Table 4. Results on the necessary amount of NG in a CHP process to replace the DO consumed in Novo Hamburgo's industrial sector

	2013	Base unit
DO consumed	4.142.637	l (liters)
Electricity generated by DO	1.077.086	kWh
NG needed to generate the same amount of electricity	3.590.285	m^3
NG in a cogeneration process needed to generate the same amount of electricity	2.333.686	m^3

4.3 CO_2 emissions reduction evaluation

According to the method used it was possible to measure DO emission in 2013: 11,061 $GgCO_2$. So, if we replaced the fuel used in the industrial sector for NG, the total annual NG emission would be: 4,541 $GgCO_2$. Fig. 6 shows the total emission of each fuel type by considering the time estimated for the project (10 years).

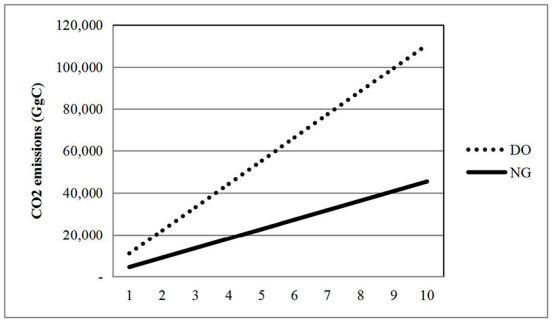

Figure 6. Total CO_2 emission by fuel type

We found that at the end of the project (considering a 10 year period) we estimate 65,196 $GgCO_2$ or 6,520 $GgCO_2$/year (6.52 $MtCO_2$/year) on emissions savings. So, the difference of using a NG CHP system presents approximately 60% lesser GHG emission than that using DO.

5. Conclusion

Diesel replacement to natural gas can be a powerful instrument to achieve integration between decentralized energy generation and energy-efficient initiatives. Thus, CHP is a potential technical solution to be explored in the integration of energy generation initiatives in the industrial sector of Brazilian cities.

A comparative analysis of the DO use and replacement by NG in a CHP system at the municipal industrial sector was performed due to such opportunity. It was estimated that the mechanical, chemical, textile, metallurgical, food and beverage industries in Novo Hamburgo consume a lot of power and heat in their industrial processes; therefore, they are suitable for the use of cogeneration systems.

In addition, it was estimated that if NG replaces the current electricity generation by DO in cogeneration systems in Novo Hamburgo's industrial sector, NG consumption in 2013 would have been almost half of the DO consumption.

An evaluation of CO_2 emissions and the difference in using a NG cogeneration system on GHG emissions is approximately 60% lower than the emissions of CO_2 from DO, representing a reduction of 6.52 $MtCO_2$/year.

Such difference in the industrial activities will benefit the environment as a whole and the people who live in Novo Hamburgo since it will be good to their health, due to the decrease in the emission of hazardous gases.

Therefore, the results showed that the replacement by cogeneration plants fueled by NG in the studied industries, it is a suitable solution from an energetic, economic and environmental point of view. Public policies should play an important role in promoting investments in order to increase NG consumption in Novo Hamburgo's the industrial sector. In addition, we recommend studies that compare those systems combined with renewable resources (solar, wind, biomass, hydro-electric power) in order to improve the cleaner energy practices in this city.

Acronyms

C	Carbono	IP	installed power
CA	carbon amount	J	Joule
CH4	Methane	J	time considered in years
CHP	combined heat and power	LHV	lower heating value
CO2	carbon dioxide	N2O	nitrous oxide
ConvF	conversion factor	NCE	net carbon emissions
CorrF	correction fator	NG	natural gas
DO	diesel oil	NGc	natural gas consumption
DOt	total diesel oil consumption	NGco	natural gas in a cogeneration system necessary to substitute diesel oil
EC	energy consumption	OFC	oxidized carbon fraction
EE	electric energy generated per year	PM	particulate matter
EmissF	emission fator	RCE	real carbon emissions
FCA	fixed carbon amount	RECO2	real carbon dioxide emissions
G	Giga	T	Terá
GHG	greenhouse gases	T	Tons
HHV	higher heating value	toe	tonne of oil equivalente
ICE	internal combustion engine		

 DOI: https://doi.org/10.30564/jasr.v2i1.419

References

[1] Brito, T. L. F.; Galbieri, R.; Mouette, D.; Costa, H. K. M; Moutinho Dos Santos, E.; Faga, M. T. W. (2017), Bus fleet emissions: new strategies for mitigation by adopting natural gas. Mitigation and Adaptation Strategies for Global Change, v. 23, p. 147-160.

[2] Brito, T. L. F.; Moutinho dos Santos, E.; Galbieri, R.; Costa, H. K. M. (2016), Qualitative Comparative Analysis of cities that introduced compressed natural gas to their urban bus fleet. Renewable & Sustainable Energy Reviews, p. 502-508.

[3] Lovins, A. (2011), Reinventing Fire: Bold Business Solutions for the New Energy Era. Rock Mountain Institute. Chelsea Green Publishing, USA.

[4] Collaço, F.M.A., Weber, N.A.B., Costa, H.K.M., Santos, E.M., Bermann, C. (2016), How decentralized energy planning can contribute to cleaner production initiatives, p. 209-228. In: Biagio, F., Giannetti, C.M.V.B., Almeida, F.A., Sevegnani, F. Advances in Cleaner Production, NY, Nova Publisher, v. 2.

[5] Andreos, R. (2013), Estudo de viabilidade técnico-econômica de pequenas centrais de cogeração a gás natural no setor terciário do estado de São Paulo. Dissertação de Mestrado. Programa de Pós Graduação em Energia (EP/FEA/IEE/IF). São Paulo.

[6] Driesen, J., Katiraei, F. (2008), Design for Distributed Energy Resources. IEEE power & energy magazine, v. 6, p. 1540-7977.

[7] Ren, H., Gao, W. A. Milp (2010), model for integrated plan and evaluation of distributed energy systems. Applied Energy, v. 87, p. 1001–1014.

[8] Doluweera, G.H., Jordaan, S.M., Moore, M.C., Keith, D.W., Bergerson, J.A. (2011), Evaluating the role of cogeneration for carbon management in Alberta G.H. Energy Policy, v. 39, p. 7963–7974.

[9] Moya, J. A. (2013), Impact of support schemes and barriers in Europe on the evolution of cogeneration. Energy Policy, v. 60, p. 345–355.

[10] Siler-Evans, K., Morgan, M. G., Azevedo, I.L. (2012), Distributed cogeneration for commercial buildings: Can we make the economics work? Energy Policy, v. 42, p. 580–590.

[11] Korhonen, J. (2002), A material and energy flow model for co-production of heat and power. Journal of Cleaner Production, v. 10, p.537-544.

[12] Ouellette, A., Rowe, A., Sopinka, A., Wild, P. (2014), Achieving emissions reduction through oil sands cogeneration in Alberta's deregulated electricity market. Energy Policy, v. 71, p. 13–21.

[13] Baer, P., Brown, M.A., Kimb, G. (2015), The job generation impacts of expanding industrial cogeneration. Ecological Economics, v. 110, p. 141–153.

[14] Andrews, D., Riekkola, A.K., Tzimas, E. (2012), Background Report on EU-27 District Heating and Cooling Potentials, Barriers, Best Practice and Measures of Promotion. Luxem- bourg.

[15] Chittum, A., Østergaard, P.A. (2014), How Danish communal heat planning empowers municipalities and benefits individual consumers. Energy Policy, v. 74, p. 465–474.

[16] Connolly, D., Lund, H., Mathiesen, B.V., Werner, S., Möller, B., Persson, U., Boermans, T., Trier, D., Østergaard, P.A., Nielsen S. (2014), Heat roadmap Europe: combining district heating with heat savings to decarbonise the EU energy system. Energy Policy, v. 65, p. 475–489.

[17] Tian, J., Liu, W., Lai, B., Li X., Chen, L. (2014), Study of the performance of eco-industrial park development in China. Journal of Cleaner Production, v. 64, p. 486-494.

[18] Iacobescu, F., Badesc, V. (2011), Metamorphoses of cogeneration-based district heating in Romania: A case study. Energy Policy, v. 39, p. 269–280.

[19] Rutter, P., Keirstead, J. (2012), A brief history and the possible future of urban energy systems. Energy Policy, v. 50, p. 72–80.

[20] Chung, M., Park, C., Lee, S., Park, H.C., Hoonim, Y., Chang, Y. (2012), A decision support assessment of cogeneration plant for a community energy system in Korea. Energy Policy, v. 47, p. 365–383.

[21] Celador, C., Erkoreka, A., Escudero K., Sala, J.M. (2011), Feasibility of small-scale gas engine-based residential cogeneration in Spain. Energy Policy, v. 39, p. 3813–3821.

[22] Palomino, R.G., Nebra, S.A. (2012), The potential of natural gas use including cogeneration in large-sized industry and commercial sector in Peru. Energy Policy, v. 50, p. 192–206.

[23] COGEN. Associação da Indústria de Cogeração de Energia. 2015. Available at: http://www.cogen.com.br/ (Accessed 15.10.2015).

[24] Hwang, J. J. (2012), Thermal regenerative design of a fuel cell cogeneration system. Journal of Power Sources, v. 219, p. 317 and 324.

[25] Karschin, I.; Geldermann, J. (2015), Efficient cogeneration and district heating systems in bioenergy villages: an optimization approach. Journal of Cleaner Production, v. 104, p. 305- 314.

[26] Ravina, M.; Genon, G. (2015), Global and local emissions of a biogas plant considering the production of biomethane as an alternative end-use solution. Journal of Cleaner Production, v. 102, p.115- 126.

[27] Celma, A. R., Blázquez, F. C., Rodríguez, F.L. (2013),

DOI: https://doi.org/10.30564/jasr.v2i1.419

Feasibility analysis of CHP in an olive processing industry. Journal of Cleaner Production, v. 42, p. 52-57.

[28] Andersen, A.N., Lund, H. (2007), New CHP partnerships offering balancing of fluctuating renewable electricity productions. Journal of Cleaner Production, v. 15, p. 288-293.

[29] Aldrich, R., Xavier, F., Puig, J., Mutjé, P., Pèlach, M. (2011), Allocation of GHG emissions in combined heat and power systems: a new proposal for considering inefficiencies of the system. Journal of Cleaner Production, v. 19, p.1072-1079.

[30] Moloney, S., Horne, R. E., & Fien, J. (2010). Transitioning to low carbon communities—from behaviour change to systemic change: Lessons from Australia. Energy policy, 38(12), 7614-7623.

[31] Fahlén, E.; Ahlgren, E. (2012), Accounting for external environmental costs in a study of a Swedish district-heating system e an assessment of simplified approaches. Journal of Cleaner Production, v. 27, p. 165- 176.

[32] Weber, N. (2014), Levantamento e análise de dados para diagnóstico energético do município de Novo Hamburgo. Trabalho de conclusão de curso. Engenharia em Energia. Universidade Estadual do Rio Grande do Sul (UERGS), Novo Hamburgo.

[33] Korhonen, J. (2001), Co-production of heat and power: an anchor tenant of a regional industrial ecosystem. Journal of Cleaner Production, v. 9, p. 509-517.

[34] IPCC. Revised 1996 IPCC Guidelines for National Green House Gas Inventories. 1996. Available at: http://www.ipcc-nggip.iges.or.jp/public/gl/invs1.html (Accessed 10.10.2015).

[35] ELETROBRAS. Inventário de Emissões de Gases de Efeito Estufa provenientes de Usinas Termelétricas (fontes fixas): 2003 a 2008. 2009. Available at: http://www.eletrosul.gov.br/files/files/sustentabilidade/gestao-ambiental/INVENT%C3%81RIO_DE_EMISS%C3%95ES_DE_GEE_UTES_2003_2008%5B1%5D.pdf (Accessed 15.10.2015).

[36] Ribeiro, L. S. O Impacto do Gás Natural nas Emissões de Gases de Efeito Estufa: o Caso do Município do Rio de Janeiro. 2003. Available at: http://www.ppe.ufrj.br/ppe/production/tesis/lsribeiro.pdf [Accessed 15.10.2015].

[37] Associação Comercial, Industrial E De Serviços De Novo Hamburgo, Campo Bom E Estância Velha, Aci-Novo Hamburgo/Cb/Ev, 2015. Data sent by e-mail (18.09.2015).

[38] Martins, C. M. R., 2013. Caracterização da Região Metropolitana de Porto Alegre. 2013. Available at: http://cdn.FUNDAÇÃO DE ECONOMIA E ESTATÍSTICA.tche.br/tds/112.pdf (Accessed 28.09.2014).

[39] Capeletto, G., 2014. Balanço Energético do Rio Grande do Sul 2014: ano base 2013.http://www.ceee.com.br/pportal/ceee/archives/BERS2013/Balanco_Energetico_RS_2014_base_2013.pdf (Accessed 21.10.2015).

[40] SULGÁS. Com a cogeração, você pode obter maior aproveitamento energético. 2015. Available at: www.sulgas.rs.gov.br/sulgas/index.php/cogeracao (Accessed 20.10.2015).

 DOI: https://doi.org/10.30564/jasr.v2i1.419

BILINGUAL PUBLISHING CO.
Pioneer of Global Academics Since 1984

Journal of Atmospheric Science Research
http://ojs.bilpublishing.com/index.php/jasr

ARTICLE

Assemble of Dye Sensitized Solar Cell Based on Locally Available Natural Dye

Samia Tabassum Ayesha Siddika Munira Sultana Mashudur Rahaman
Muhammad Shahriar Bashar*

Institute of Fuel Research and Development, Bangladesh Council of Scientific and Industrial Research, Dhaka, Bangladesh

ARTICLE INFO

Article history
Received: 9 January 2019
Accepted: 15 January 2019
Published: 28 February 2019

Keywords:
Natural dye
Anthocyanin
Photo anode
Electrolyte
Efficiency

ABSTRACT

Due to the availability, non-toxicity and cost-effectivity, natural dyes are becoming popular day by day. This study explains the fabrication method of dye-sensitized solar cells (DSSCs) using natural dyes containing anthocyanins extracted from pomegranate, blackberry and beetroot. Doctor blade method was employed to prepare TiO_2 film as photoanode on FTO glass. The structural and morphological properties of photoanode was studied using X-ray diffraction (XRD) and Scanning Electron Microscopy (SEM), respectively. The extracted dye absorption was evaluated by UV-Vis-NIR spectroscopy. The fabricated cells have efficiency in the range of 0.015-0.042% which has been measured by sun simulator.

1. Introduction

The replacement of fossil fuel with renewable energy sources is extremely needed in this time in order to reduce global warming which causes climate change. Also, the storage of fossil fuel supply is decreasing every year. Solar energy is an alternative unlimited energy source which can be utilized to generate electricity. Dye Sensitized Solar Cell (DSSC) is the third-generation photovoltaic solar cell which has achieved huge attention in recent years. Grätzel is the pioneer of DSSC fabrication [1]. DSSC is actually bio mimicry of light dependent photosynthesis process of plants and uses artificial photosynthesis method. Photosynthesis is the process used by plants to convert light energy into chemical energy. The similar principle applied in the construction of Dye Sensitized Solar Cell (DSSC) [2].

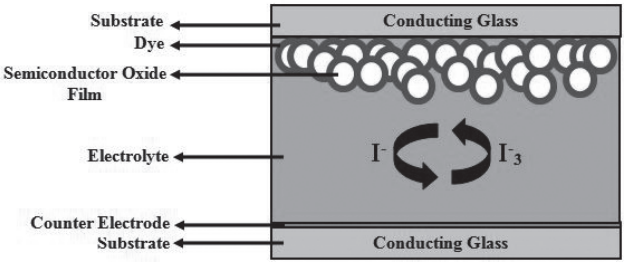

Figure 1. Schematic Representation of Dye Sensitized Solar Cell

The schematic representation of dye sensitized solar cell is demonstrated in Figure 1. In the dye sensitized solar

**Corresponding Author:*
Muhammad Shahriar Bashar,
Institute of Fuel Research and Development, Bangladesh Council of Scientific and Industrial Research, Dhaka, Bangladesh
E-mail: shawon14@gmail.com

 DOI: https://doi.org/10.30564/jasr.v2i1.469

cell, the semiconductor layer with large band gap acts as photoanode. After photo excitation, dye molecules infuse excited electrons into the conduction band of the nano-structured film and get oxidized. The injected electron is then transported to the external circuit. By collecting electrons from the electrolyte, the oxidized dye molecules get revived. Therefore, I- ion then become I^-_3. Then the I^-_3 reduced back to I- ion by gaining electrons from external circuit [3,4]. There are different developed techniques for photoanode deposition, such as sol gel [5], Hydrothermal [6], Solvothermal [7], Spin Coating Deposition [8,9], Doctor Blade Method [10], screen printing method [11]. TiO_2, ZnO, Nb_2O_5, SnO_2 are used as photo anodes [12-15]. However, $SrCO_3$, Al_2O_3, La_2O_3 etc. can be acted as insulating layer to prevent charge reassemble and improve power conversion efficiency [16-18]. Different types of natural and synthetic dyes are used as sensitizers [19-22]. The inexpensive natural dyes are more attractive compared to the synthetic dyes, because, they are abundant in supply and environmentally friendly. On the other hand, synthetic dye is very costly though the performance of DSSC using synthetic dye showed the higher efficiency. The red ox electrolyte reestablishes the initial state of the dye consequently [4]. The iodide triiodide (I_3^-/I^-) electrolyte is a ubiquitous redox transporter. The ability to reform dye by quick oxidation of I^- at the photo anode/electrolyte terminal and high charge collection by slow reduction of I_3^- at the electrolyte/counter electrode terminal has made this electrolyte ideal for DSSC. It is also very attractive because of its good penetration, cost effective and better sustainability[23]. The counter electrode accumulates charges from the exterior circuit and injects back to the circuit loop in the cell. Highly conductive and very stable materials are strongly recommended as counter electrode materials [24]. The most popular counter electrodes for DSSC are Pt, Au and Ag. Moreover, several kinds of inorganic compounds, composites are also used as counter electrode because of the expensiveness of the noble metals.

Many researches have been established upon the different layers in order to escalate the performance of the DSSC solar cell. In this work, DSSC has been prepared using natural dye extract from blackberry, beet and pomegranate. These dyes have been selected, because they are easily obtainable in the regional market and they are cost effective. The dye absorption spectrum, structural, morphological property of TiO_2 and DSSC efficiency has been then investigated.

2. Experimental

2.1 Preparation of TiO_2 Film

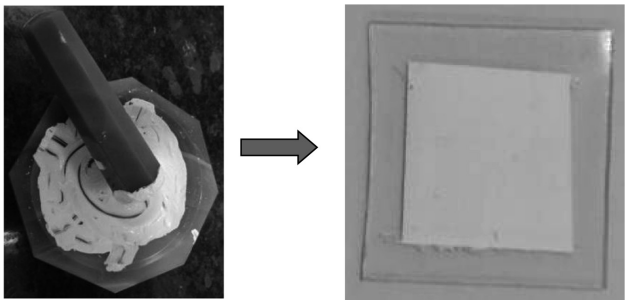

Figure 2. TiO_2 film preparation method

Since the photo-anode generates charge and process to transfer, so, it is very important part in DSSC. In this research, TiO_2 film was prepared by using doctor blade method. At first, TiO_2 powder was grinded for 1 hr in a mortar. HNO_3 (1:1) was dropped into the powder and mix it vigorously. FTO glass with resistance less than 10 ohm was ultrasonically cleaned in ethanol and acetone. The obtained TiO_2 paste was spread onto clean FTO glass by glass stirring rod. The samples were dried at room temperature for 30 min. The TiO_2 coated FTO was then annealed at 450°C for 30 min due to remove organic substances from the samples and make it crystalline. As the temperature is less than 700°C, the prepared TiO_2 film is expected to form anatase [25]. Annealing of this film can improve surface morphology and crystallinity. After annealing, the film coated with TiO_2 is ready to absorb the dye solution.

2.2 Dye Extraction

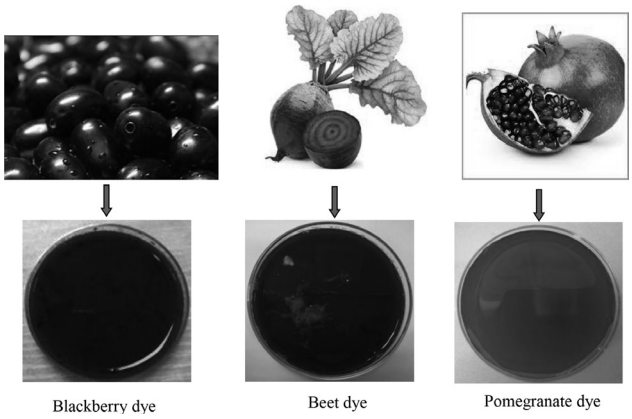

Figure 3. Dye extraction from different fruits

Natural dye including anthocyanin is used as sensitizer in DSSC. This compound is present in many flowers, leaves and fruits. In this experiment, three different types of dyes were extracted from blackberry, pomegranate and beet root which is shown in Figure 3. These raw materials were collected from the local market and washed to reduce the dust particles. Here, we used only the skin for

DOI: https://doi.org/10.30564/jasr.v2i1.469

blackberry. By using mortar, the pure juice was extracted from blackberry skin. Similar procedures were applied for pomegranate except the grinding method (hand grinding method was applied). Beet root is little bit hard and to extract the dye, DI was used to blend in the ratio of 1:1. The extracted dye was filtered through net and then filter paper to obtain clear dye. TiO_2 films were dipped into the extracted dye for overnight. It was covered with aluminum foil and kept in dark places.

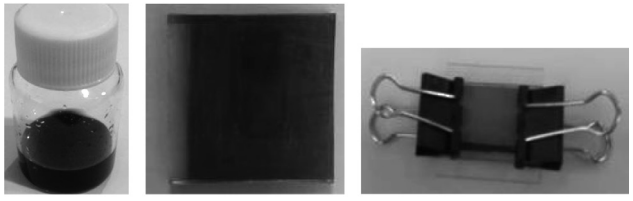

Electrolyte Counter electrode Assembled DSSC

Figure 4. Electrolyte, counter electrode and assembled DSSC

2.3 Assemble of Dye Sensitized Solar Cell

After whole night absorption the film was rinsed with DI water to remove unabsorbed dye and other remains which present on the surface. Then it was dried in air. At the same time, another FTO glass was cleaned and conductive side of the glass was coated by carbon with the assist of 10B pencil which acts as counter electrode. Due to assembly of DSSC, TiO_2 coated glass slide which was immersed in dye was set in face to face with carbon coated glass slide. The two electrodes were assembled together using binder clips by keeping electrical contacts in both sides. To prepare the electrolyte solution Potassium Iodide, Iodine and Ethelene Glycol have been used. 0.5M KI and 0.05M I_2 was dissolved in Ethelene Glycol solvant and stirred for 30 minutes in a magnetic stirrer. This electrolyte Iodolite solution was introduced between two electrodes and penetrated into the cell. The assembled DSSC is shown in Figure 4.

3. Result and Discussion

TiO_2 nano-crystalline semiconductor film was deposited onto FTO glass by doctor blade method and annealed at 450°C in a furnace. The thickness of the film was measured by surface profilometer and which was 18 nm. To observe the crystalline structure, XRD patterns of the TiO_2 layer is shown in Graph 1. The film is polycrystalline and anatase phase of TiO_2 which satisfy the standard data of JCPDS card no. 21-1272. The strong diffraction peak appears of (101) at 25.5°. The others peak position at 38°, 48°, 54°, 56°, 63° corresponding of (004), (200), (105), (204) planes are in accordance with the TiO_2 anatase phase. The XRD pattern of TiO_2 film with exhibited peaks corresponding to anatase phase indicates the presence of stable TiO_2 film.

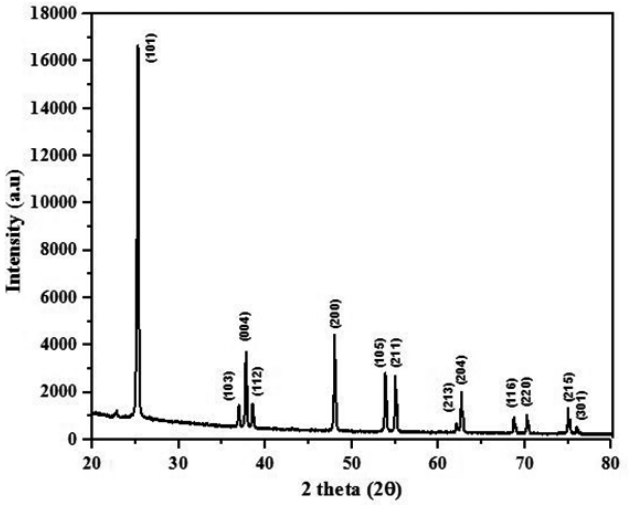

Graph 1. XRD curve of TiO_2 thin film

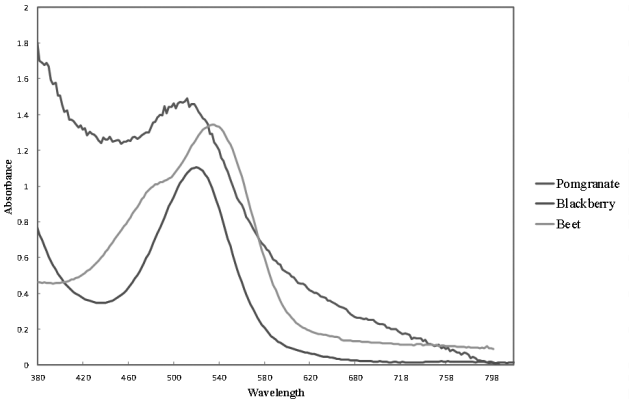

Graph 2. Absorption spectra of different dyes

The overall performance of a DSSC is also dependent on the sensitizer which is capable to absorb light. The absorption of the dye extracted from blackberry, pomegranate and beetroot was investigated using UV-vis spectrometry. Dye was diluted with water before measurement. The absorption spectrum of the extracted dye was recorded in the visible wavelength range between 500-600 nm with a maximum absorption wavelength at 512 nm for pomegranate, 522 nm for blackberry and 536 nm for beetroot. These absorption peaks correspond to anthocyanin. It is reported that anthocyanin absorbs in the region between 500 and 600 nm. So, our result specifies the major components of the observed pigments and which is anthocyanin [26]. Apart from main peak, one more peak at 480 nm are also visible in the beet dye which indicates the presence of small amount of chlorophyll.

 DOI: https://doi.org/10.30564/jasr.v2i1.469

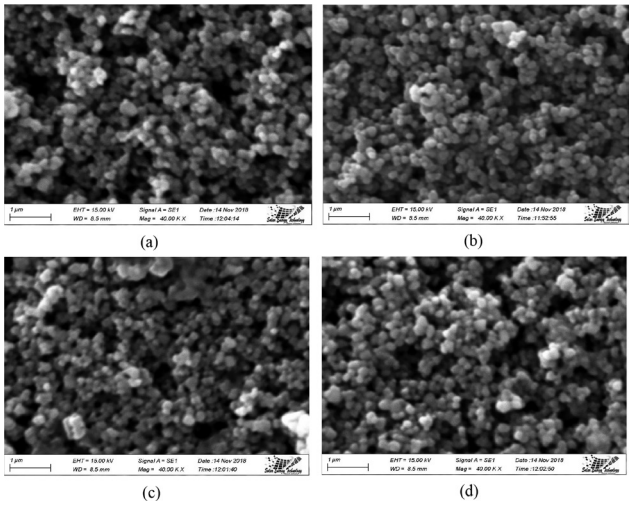

Figure 5. SEM of (a) TiO_2 film (b) TiO_2+blackberry (c) TiO_2+Beet and (c) TiO_2+pomgranate

Fig. 5(a) shows an electron micrograph of TiO_2 film. The TiO_2 film had spherical form and distributed almost uniformly with particle sizes ranging from 0.2-0.3 μm. Figure shows the porous electrode with high specific surface area. The surface of photo electrode is very significant as the chemical reactions performed mainly on the surface of the photocatalyst. TiO_2 film was kept into the dye. It was expected to observe the changes in surface morphology after dye absorption. But there were no significant changes were noticed in that case. But these SEM micrographs indicate some minimization of holes by adsorbing dye on to the TiO_2 nanoparticles.

Table 1. I-V measurements of DSSC prepared using different dyes

	Voc (V)	Isc (mA/cm2)	Fill factor (%)	Efficiency (%)
Blackberry	0.373	0.892	25.06	0.029
Pomegranate	0.425	0.81	29.44	0.042
Beet route	0.383	0.323	35.11	0.015

The efficiency of DSSC was measured by exposing in the sun simulator under the irradiance of the equal sun. Table-1 summarize the information about the performance of different dyes as sensitizer via the current, voltage, fill factor and conversion efficiency. The fill factor of the DSSCs is varied from 25 to 35%, The Voc and Isc ranges from 0.373 to 0.425 V and 0.323 to 0.892 mA/cm2, respectively. The cell prepared by using pomegranate dye exhibited the highest light to electric energy conversion efficiency of 0.042%.

4. Conclusion

In this work, locally available natural dyes extracted from pomegranate, blackberry and beetroot have been used as sensitizers in dye sensitized solar cells. The dye solutions contain anthocyanin which is a good source of sensitizer. Dye molecules adsorbed into TiO_2 thin film coated onto FTO glass which act as a photoanode. This film was sandwiched by carbon coated FTO glass counter electrode. DSSC assembling was fulfilled by inserting electrolyte in between them. It was found that DSSC prepared with pomegranate dye is more efficient than other dyes (where, Voc of 0.425 V, Isc of 0.81 mA/cm2 and power conversion efficiency of 0.042%). Natural dyes used in this experiment are locally available and solar cell fabrication method is easy and cheap also. Due to these reasons these dyes which act as sensitizer or light harvesting materials could be promising candidate for DSSC.

References:

[1] Michael Grätzel, Dye-sensitized solar cells [J]. Journal of Photochemistry and Photobiology C: Photochemistry Reviews, 4 2003 145–153 (10.1016/S1389-5567(03)00026-1).

[2] Khalil Ebrahim Jasim. Dye Sensitized Solar Cells - Working Principles, Challenges and Opportunities [M]. (10.5772/19749).

[3] Anders Hagfeldt, Gerrit Boschloo, Licheng Sun, Lars Kloo, and Henrik Pettersson, Dye-Sensitized Solar Cells [J]. Chemical Reviews, 110, 2010, 6595–6663 (10.1021/cr900356p).

[4] Meidan Ye, Xiaoru Wen, Mengye Wang, James Iocozzia, Nan Zhang, Changjian Lin, and Zhiqun Lin. Recent advances in dye-sensitized solar cells: from photoanodes, sensitizers and electrolytes to counter electrodes [J]. Materials Today, Volume 18, Number 3 , April 2015 (10.1016/j.mattod.2014.09.001).

[5] Yu-Chang Liu, Yun-Fang Lu, Yz-Zhen Zeng, Chi-Hung Liao, Jen-Chieh Chung, and Tsong-Yang Wei. Nanostructured Mesoporous Titanium Dioxide Thin Film Prepared by Sol-Gel Method for Dye-Sensitized Solar Cell [J]. International Journal of Photoenergy, Volume 2011, Article ID 619069, 9 pages (10.1155/2011/619069).

[6] Varishetty Madhu Mohan and Kenji Murakami. Hydrothermal Synthesis of TiO_2 Porous Hollow Nanospheres for Coating on the Photoelectrode of Dye-Sensitized Solar Cells [J]. Japanese Journal of Applied Physics 51, 2012, 2052–2061 (10.1143/JJAP.51.02BP11).

[7] J. Archana, M. Navaneethan, Y. Hayakawa. Solvothermal growth of high surface area mesoporous anatase TiO_2 nanospheres and investigation of dye-sensitized solar cell properties [J]. Journal of Power Sources, 242, 2013, 803-810(10.1016/j.jpowsour.2013.05.126).

DOI: https://doi.org/10.30564/jasr.v2i1.469

[8] S. N. Sadikin, M. Y. A. Rahman , A. A. Umar, M. M. Salleh. Effect of Spin-Coating Cycle on the Properties of TiO_2 Thin Film and Performance of DSSC [J]. International Journal of Electrochemical. Science, 12, 2017, 5529 – 5538(10.20964/2017.06.57).

[9] T. S. Senthil and Misook Kang. Transparent Thin Film Dye Sensitized Solar Cells Prepared by Sol-Gel Method [J]. Bulletin of Korean Chemical Society, Vol. 34, No. 4, 2013(10.5012/bkcs.2013.34.4.1188).

[10] Tan-Phat Huynh, Thi-Thao Hoan, Phuoc-Hiep Nguye, Thanh-Nam Tran, The-Vinh Nguyen,. Preparation of TiO_2 thin film using modified doctor-blade method for improvement of dye-sensitized solar cell [J]. (10.1109/PVSC.2009.5411405)

[11] Agus Supriyanto , Lutfi Furqoni , Fahru Nurosyid , Jojo Hidayat , Risa Suryana, Effect of sintering temperatures and screen printing types on TiO_2 layers in DSSC applications [J]. AIP Conference Proceedings 1717, 2016, 040001 (10.1063/1.4943444).

[12] Kazuya Nakataa, Akira Fujishima. TiO_2 photo catalysis: Design and applications [J]. Journal of Photochemistry and Photobiology C: Photochemistry Reviews 13, 2012 169–189 (10.1016/j.jphotochemrev.2012.06.001).

[13] Seung Hwan Ko, Daeho Lee, Hyun Wook Kang, Koo Hyun Nam, Joon Yeob Yeo, Suk Joon Hong, Costas P. Grigoropoulos and Hyung Jin Sung. Nanoforest of Hydrothermally Grown Hierarchical ZnO Nanowires for a High Efficiency Dye-Sensitized Solar Cell [J]. Nano Letters, 11, 2011, 666–671(10.1021/nl1037962).

[14] Haimin Zhang, Yun Wang, Porun Liu, Shu Lei Chou, Jia Zhao Wang, Hongwei Liu, Guozhong Wang, and Huijun Zhao. Highly Ordered Single Crystalline Nanowire Array Assembled Three-Dimensional Nb3O7(OH) and Nb2O5 Superstructures for Energy Storage and Conversion Applications [J]. ACS Nano. 10(1), 2016 Jan 26, 507-14 (10.1021/acsnano.5b05441).

[15] Zhengdao Li, Yong Zhou, Ruzhong Sun, Yan Xiong, Haiquan Xie, Zhigang Zou. Nanostructured SnO_2 photoanode-based dye-sensitized solar cells [J]. Chinese Science Bulletin, 59, 18, 2014, 2122–2134 (10.1007/s11434-013-0079-3).

[16] Shutao Wang, Xi Zhang, Gang Zhou and Zhong-Sheng Wang. Double-layer coating of $SrCO_3/TiO_2$ on nanoporous TiO_2 for efficient dye-sensitized solar cells [J]. Physical Chemistry Chemical Physics, 14, 2012, 816–822 (10.1039/c1cp23041g).

[17] Xianfeng Gao, Dongsheng Guan, Jingwan Huo, Junhong Chen and Chris Yuan. Free standing TiO_2 nanotube array electrodes with an ultra-thin Al_2O_3 barrier layer and TiCl4 surface modification for highly efficient dye sensitized solar cells [J]. Nanoscale, 5, 2013, 10438–10446 (10.1039/c3nr03198e).

[18] Hua Yu, Bofei Xue, Porun Liu, Jingxia Qiu, William Wen, Shanqing Zhang and Huijun Zhao. High-Performance Nanoporous TiO_2/La_2O_3 Hybrid Photoanode for Dye-Sensitized Solar Cells [J]. ACS Appllied Materials and Interfaces, 4, 2012, 1289−1294 (10.1021/am2015553).

[19] Khwanchit Wongcharee, Vissanu Meeyoo, Sumaeth Chavadej. Dye-sensitized solar cell using natural dyes extracted from rosella and blue pea flowers [J]. Solar Energy Materials and Solar Cells , 91, 7, 16 April 2007, 566-571(10.1016/j.solmat.2006.11.005).

[20] Ho Chang , Yu-Jen Lo. Pomegranate leaves and mulberry fruit as natural sensitizers for dye-sensitized solar cells [J]. Solar Energy, 84, 2010, 1833–1837 (10.1016/j.solener.2010.07.009).

[21] F. Teoli, S. Lucioli, P. Nota, A. Frattarelli, F. Matteocci, A.Di Carlo, E. Caboni, C. Forni . Role of pH and pigment concentration for natural dye-sensitized solar cells treated with anthocyanin extracts of common fruits [J]. Journal of Photochemistry and Photobiology A: Chemistry, 316, 2016, 24–30 (10.1016/j.jphotochem.2015.10.009).

[22] Yuancheng Qin and Qiang Peng . Ruthenium Sensitizers and Their Applications in Dye-Sensitized Solar Cells [J]. International Journal of Photoenergy Volume 2012, Article ID 291579, 21 pages (10.1155/2012/291579).

[23] Mingkui Wang, Carole Grätzel, Shaik M. Zakeeruddin and Michael Grätzel. Recent Developments in Redox Electrolytes for Dye-Sensitized Solar Cells [J]. Energy and Environmental Science, 5, 2012, 9394-9405 (10.1039/C2EE23081J).

[24] Yung-Sheng Yen, Hsien-Hsin Chou, Yung-Chung Chen, Chih-Yu Hsu and Jiann T. Lin. Recent developments in molecule-based organic materials for dye-sensitized solar cells [J]. Journal of Materials Chemistry, 2012, 22, 8734(10.1039/c2jm30362k).

[25] F.I.M. Fazli, N. Nayan, M.K. Ahmad, M.L.Mohd Napi, N.K.A. Hamed & N.S. Khalid. Effect of annealing temperatures on TiO_2 thin films prepared by spray pyrolysis deposition method [J]. Sains Malaysiana, 45(8), 2016, 1197-1200.

[26] Wuletaw Andargie Ayalew, Delele Worku Ayele. Dye-sensitized solar cells using natural dye as light-harvesting materials extracted from Acanthus sennii chiovenda flower and Euphorbia cotinifolia leaf [J]. Journal of Science: Advanced Materials and Devices, 1, 2016, 488-494(10.1016/j.jsamd.2016.10.003).

 DOI: https://doi.org/10.30564/jasr.v2i1.469

BILINGUAL PUBLISHING CO.
Pioneer of Global Academics Since 1984

Journal of Atmospheric Science Research
http://ojs.bilpublishing.com/index.php/jasr

REVIEW

Design Scheme of Electric Lifting Workbench for Maintenance of Aerometer in Observation Field

Haitao Yan

Meteorological Bureau of Tai'an City, Shandong Province, Tai'an, 271000, People's Republic of China

ARTICLE INFO

Article history
Received: 3 January 2019
Accepted: 3 January 2019
Published: 28 February 2019

Keywords:
Observation field
Wind maintenance
Electric lifting table
Design scheme

ABSTRACT

The wind speed and wind direction meter of meteorological station is installed on the wind meter pole 10 meters high from the observation site, which also causes some difficulties for the maintenance of the wind speed and wind direction meter in the later period. Based on this situation, an electric lifting worktable (referred to as the electric lifting worktable) is specially designed for the maintenance of wind meters in meteorological observation sites. It can lift the maintenance personnel and equipment and tools to a height convenient for work, and then grasp the wind meter pole through the mechanical arm. It can be operated by a single person, thus getting rid of the traditional dimension by climbing the wind meter pole or releasing the wind meter pole. The present situation of repairing has the characteristics of saving manpower and easy operation, which is conducive to improving work efficiency and reducing work intensity. It also greatly guarantees the safety of maintenance personnel, and has good practicability and extensive popularization value.

Classification Number of Chinese Map: P414

1. Introduction

The induction part of the wind meter in the meteorological station is installed on the wind meter pole 10 meters above the ground[1]. Nowadays, most of the wind meter sensors are replaced or repaired by putting the wind meter pole upside down. The labor intensity is high, and it is impossible for a single person to carry out maintenance operation, so it is inconvenient to carry out emergency repair, which brings many difficulties to the maintenance work. In view of this situation, an electric lifting worktable for maintenance of wind meters in meteorological observation sites is designed[2]. The worktable is safe and reliable. It can raise the maintenance worktable to a height convenient for maintenance work under the condition of full relaxation of hands, feet and body. It can be operated by a single person, which is convenient for timely repair of wind meters and can relieve the general meteorology. The difficulties in maintaining wind meters at stations are

2. Reasons for Inconvenience in Maintenance of Wind Meters

There are two main reasons for the difficulty in the maintenance of wind meters.

The wind sensor of meteorological station is installed at a height of 10 meters in the observation field, which is far beyond the height range of people's convenient work.

**Corresponding Author:*
Haitao Yan,
Meteorological Bureau of Tai'an City, Shandong Province, Tai'an, 271000, People's Republic of China
Email: 617849141@qq.com

 DOI: https://doi.org/10.30564/jasr.v2i1.443

Only by means of other devices can the wind sensor be approached for maintenance work.

At present, most meteorological stations have no pedals and top platforms. Therefore, only by putting down the wind lever to maintain it, it will cause a long maintenance process, heavy labor intensity, unable to operate by one person, which is not conducive to the timely repair of faults.

3. Solutions to the Problem of Aerometer Sensor Maintenance

To solve the difficulties caused by the installation height of the wind meter sensor, we can make a wheeled electric lifting table[3], which requires simple and convenient movement and lifting operation, safe and fast, and can operate by one person for the maintenance of the wind meter.

3.1 Design Scheme of Electric Lifting Workbench

In order to meet the above requirements and objectives, an electric lifting table for maintenance of wind meters in meteorological observation field is specially designed, which mainly includes worktable, electric lifting mechanism[4], grasping manipulator[5], control panel, base and fixed support foot mechanism[6].

3.2 Worktable

The bottom frame of the working table is welded by 600×600 mm square pipe. The thickness of the steel plate is 3 mm. The length and width of the steel plate are 600 mm and 400 mm. A guardrail is connected with the bottom frame of the working table. The guardrail is 1000mm higher than the countertop. The guardrail is welded by 50 mm diameter stainless steel pipe. A reinforcing bar is added between the longitudinal and horizontal grids of the guardrail. See figs 1 and 2. In order to facilitate the maintenance personnel to enter and leave the worktable, the upper door is installed at one end of the guardrail, and the guardrail bar is equipped with multiple hooks with buckles, so as to facilitate the suspension of toolkits and spare wind speed sensors.

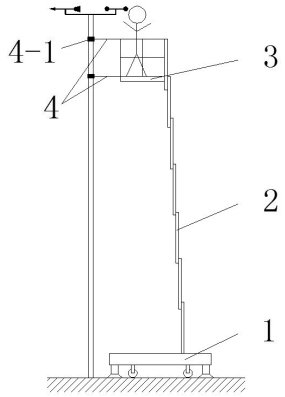

Figure 1. Schematic diagram of the observation field instrument maintenance for electric lifting table

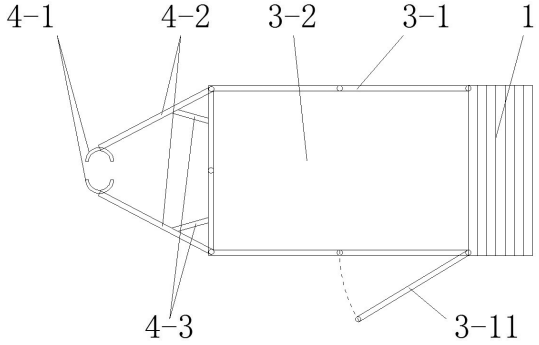

Figure 2. The overlook chart of the electric lifting table

3.3 Electric Lifting Mechanism

The electric lifting mechanism is a single mast type electric slide rail lifting mechanism, which is connected with one end of the upper worktable and the lower end with the base, as shown in Fig. 1. The single mast column adopts high strength aeronautical profile and new sliding track technology. The boom section is 200×95×6.5mm, the motor power is 1.0 kw, the load is 130 kg. The single mast column type electric sliding rail lifting mechanism can raise the working table to 10 m height.

3.4 Grab Manipulator Arm

In order to facilitate the maintenance personnel to work steadily, two pairs of grasping manipulators are arranged at one end of the worktable far from the single mast type electric lifting mechanism. Each pair of grasping manipulators includes a pair of movable connecting rods distributed along the horizontal direction and a telescopic cylinder connected with them[7]. The two pairs of grasping manipulators are vertically distributed along the side end of the worktable far from the single mast type lifting mechanism, and the two pairs of grasping manipulators are vertically distributed along the worktable. A pair of grasping manipulators are connected with the guardrail

DOI: https://doi.org/10.30564/jasr.v2i1.443

far from the grasping end, and a pair of grasping manipulators are connected with the worktable floor far from the grasping end, as shown in figs. 1 and 2. In order to grasp the wind meter rod conveniently, a telescopic cylinder is arranged on the movable connecting rod. The telescopic cylinder is located at the end of the convergence direction

3.5 Control Panel

The control panel connects and controls the electric lifting mechanism, the grasping manipulator and the supporting foot mechanism with wires.

3.6 Base and Fixed Support Foot

The base and the fixed support foot mechanism are the foundation of the whole electric lifting table. The base is made of 60×60 mm square pipe welded and laid with 3 mm thick steel plate. The length is 1450 mm and the width is 650 mm. In order to realize the convenient movement and safe and stable operation of the base, one wheel is installed in four directions below the base for easy movement. The bottom of the base is provided with a retractable fixed support foot mechanism and fixed support. The foot mechanism is located at four corners at the bottom of the base, as shown in figs. 3 and 4. The fixed support foot mechanism is equipped with shock absorber and support foot device. Each fixed support foot mechanism is connected with the lower end of the base through the hydraulic cylinder. The fixed support foot mechanism and the hydraulic cylinder are electrically connected with and controlled by the control panel. The shock absorber is equipped with springs and air pumps. When the wind outside causes the rod shaking, the electric lifting table is grasped by grasping the mechanical arm. The wind instrument pole will also be slightly swayed by the swaying of the wind instrument pole. Most of the influence of external wind force swaying on the lifting worktable can be offset by a shock absorber. The supporting foot device includes the first supporting foot and the second.

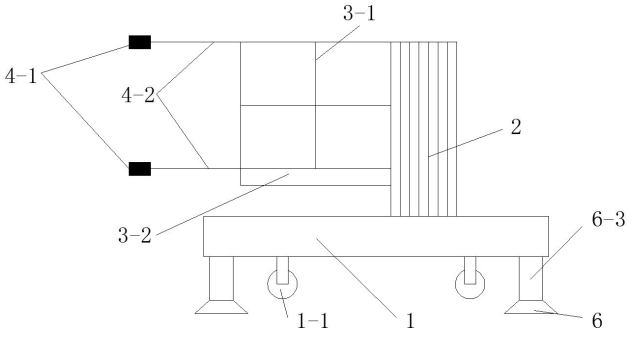

Figure 3. Schematic diagram of the structure of an electric lifting table

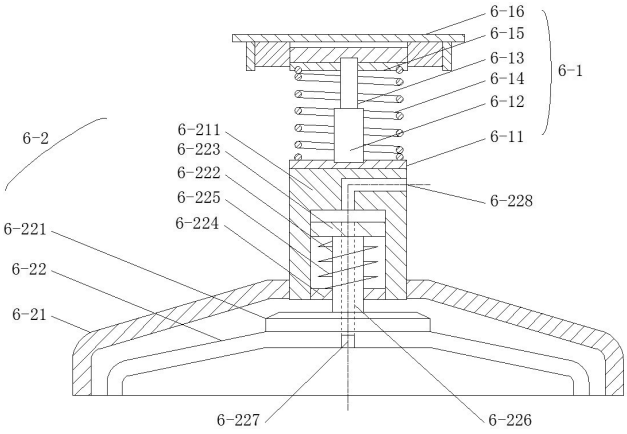

Figure 4. Schematic diagram of the structure of the supporting foot mechanism

Note: The labels in Fig. 1, Fig. 2, Fig. 3 and Fig. 4 are as follows: 1, base; 2, lifting mechanism; 3, worktable; 4, grasping manipulator arm; 5, control panel (sketch); 6, supporting foot mechanism; 3-1, guardrail; 3-2, workbench floor; 3-11. upper door; 4-1, grasp; 4-2, movable connecting rod; 4-3, telescopic cylinder; 6-1, shock absorber; 6-11, lower mounting plate; 6-12, shock absorber; 6-13, connecting rod; 6-14, first spring; 6-15, spring seat; 6-16, upper mounting plate; 6-2, supporting foot device; 6-21, first supporting foot; 6-22, second supporting foot; 6-211, cover; 6-221, connecting seat; 6-222, guide rod; 6-223, plug; 6-224, clasp; 6-225, second spring; 6-226, exhaust pipe; 6-227, relief valve, 6-228, opening.

4. The Use Method of Electric Lifting Workbench

Use Method of Electric Lifting Workbench: When it is necessary to maintain the windmill, push the electric lifting workbench to the windmill pole of the meteorological observation field. Maintenance personnel can determine the appropriate distance between the windmill pole and the windmill pole by grasping the mechanical arm through the control panel, so as to ensure that the grasping mechanical arm can still grasp the windmill pole after the workbench is raised and determine the appropriate distance. After loosening the manipulator arm and using the control panel to control the fixed support foot mechanism, the rollers are adjusted to the position after lifting off the ground with the base. After checking the loading situation of the toolkit and the necessary wind instruments, the guard door is opened to enter the workbench, and the control panel is used to control the electric lifting mechanism to raise the workbench to a height convenient to work (according to the height of each person, it is convenient to work). The height is also different). Manipulate and grasp

 DOI: https://doi.org/10.30564/jasr.v2i1.443

the manipulator arm to grasp the wind instrument pole, remove the toolkit from the guardrail hook of the worktable and replace or repair the spare wind instrument. After the repair, hang the toolkit and the changed wind instrument onto the hook, control the grasping manipulator arm by the control panel.

5. Conclusion

The electric lifting worktable for maintenance of wind meters in observation sites designed in this scheme has the advantages of simple movement, easy lifting, safety and reliability, and can be operated by single person, which is convenient for timely repair of wind meters' faults. It can save trouble in the maintenance of wind meters by putting down wind meters, reduce labor intensity, improve work efficiency, achieve the purpose of saving time and labor, and ensure safety. It can well solve the problem of wind meters' transmission in meteorological stations. The difficulty of overhaul caused by too high installation of sensors can make the hands, feet and bodies of maintenance personnel work in a state of overall relaxation. Its popularization and use will have a good role in promoting the modernization of meteorological equipment.

Reference:

[1] Drawn up by the Central Meteorological Bureau. Ground Meteorological Observation Norms [M]. Published by Meteorological Press, Beijing, 1979, 12, 1st Edition.

[2] Yan Haitao, lifting platform for maintenance of wind meters at observation sites [P]. China: ZL 2018 2 0325 866.3, 2018.

[3] Chen Jun, Chen Zhenhua, Li Suping, etc. Design and control method of wheeled mobile worktable for greeting robot [J]. Machinery Manufacturing, 2009, (11): 24-26.

[4] Xu Shufeng, He Chun. Electric Lifting Workbench [J]. Mechanical Engineer, 2009, (5): 82-83.

[5] Xu Benlian, Hou Baolin, Chen Qinglan, et al. Design and dynamics simulation of manipulator [J]. Lifting and transporting machinery, 2003, (10): 26-28.

[6] Pan Jin, Xu Fengren and Shen Zhao. Study on Static Characteristics of Self-priming Gas Supports [J]. Special Equipment for Electronic Industry, 1990, (02): 31-34.

[7] Ye Zengji, Xu Zili, Zhang Xin. Design and optimization of greeting manipulator with connecting rod transmission structure [J]. Machinery Manufacture, 2011, (05): 11-13.

DOI: https://doi.org/10.30564/jasr.v2i1.443

WITHDRAWN: High-Resolution Radiometer for Remote Sensing of Solar Flare Activity from Low Earth Orbit Satellites

Luca Aluigi

DISMI, University of Modena and Reggio Emilia, Reggio Emilia, Italy

DOI of original article: https://doi.org/10.30564/jasr.v1i1.420.

E-mail address: luca.aluigi@unimore.it (Luca Aluigi).

About the Publisher

Bilingual Publishing Co(BPC) is an international publisher of online, open access and scholarly peer-reviewed journals covering a wide range of academic disciplines including science, technology, medicine, engineering, education and social science. Reflecting the latest research from a broad sweep of subjects, our content is accessible worldwide – both in print and online.

BPC aims to provide an academic platform for academic exchange and cultural communication that help organizations and professionals in advancing society for the betterment of mankind. BPC hopes to be indexed by well-known databases in order to expand its scope to the science community, and eventually grow to be a reputable publisher recognized by scholars and researchers around the world.

BPC adopts the Open Journal Systems, see on ojs.bilpublishing.com

About the Open Journal Systems

Open Journal Systems (OJS) is sponsored by the Public Knowledge Project Organization from Columbia University in Canada, jointly developed by PKP, the Canadian Academic Publishing Center and Canada Simon Fraser University Library. OJS can realize the office automation of periodical editing process, station build and full-text journals by network publishing. The system design is in line with international standards, and supports peer review. It is very helpful to improve the citation rate, academic level and publication quality of periodicals.

Bilingual Publishing Co. is a company registered in Singapore in 1984, whose office is at 12 Eu Tong Sen Street, #08-169, Singapore 059819, enjoying a high reputation in Southeast Asian countries, even around the world.

Tel:+65 65881289
E-mail:contact@bilpublishing.com
Website:www.bilpublishing.com

BILINGUAL
PUBLISHING CO.
Pioneer of Global Academics Since 1984

ISSN 2630-5119
01
9 772630 511195